J. Fluid Mech. (2023), *vol*. 955, A4, doi:10.1017/jfm.2022.1023

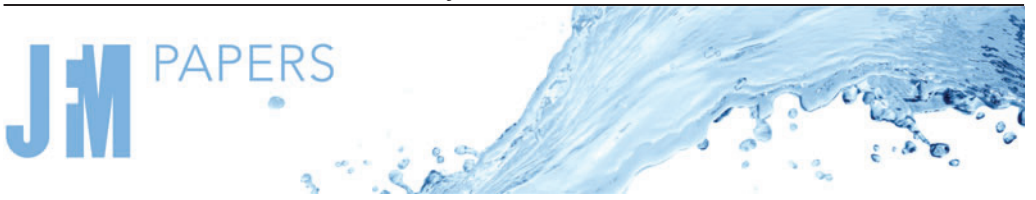

Numerical simulation of turbulent, plane parallel Couette–Poiseuille flow

W. Cheng[1],†, **D.I. Pullin**[2], **R. Samtaney**[3],‡ **and X. Luo**[1]

[1]School of Engineering Science, University of Science and Technology of China, Hefei 210027, PR China

[2]Graduate Aerospace Laboratories, California Institute of Technology, CA 91125, USA

[3]Physical Science and Engineering Division, King Abdullah University of Science and Technology, Thuwal 23955-6900, Saudi Arabia

(Received 2 July 2022; revised 17 October 2022; accepted 28 November 2022)

We present numerical simulation and mean-flow modelling of statistically stationary plane Couette–Poiseuille flow in a parameter space (Re, θ) with $Re = \sqrt{Re_c^2 + Re_M^2}$ and $\theta = \arctan(Re_M/Re_c)$, where Re_c, Re_M are independent Reynolds numbers based on the plate speed U_c and the volume flow rate per unit span, respectively. The database comprises direct numerical simulations (DNS) at $Re = 4000, 6000$, wall-resolved large-eddy simulations at $Re = 10\,000, 20\,000$, and some wall-modelled large-eddy simulations (WMLES) up to $Re = 10^{10}$. Attention is focused on the transition (from Couette-type to Poiseuille-type flow), defined as where the mean skin-friction Reynolds number on the bottom wall $Re_{\tau,b}$ changes sign at $\theta = \theta_c(Re)$. The mean flow in the (Re, θ) plane is modelled with combinations of patched classical log-wake profiles. Several model versions with different structures are constructed in both the Couette-type and Poiseuille-type flow regions. Model calculations of $Re_{\tau,b}(Re, \theta)$, $Re_{\tau,t}(Re, \theta)$ (the skin-friction Reynolds number on the top wall) and θ_c show general agreement with both DNS and large-eddy simulations. Both model and simulation indicate that, as θ is increased at fixed Re, $Re_{\tau,t}$ passes through a peak at approximately $\theta = 45°$, while $Re_{\tau,b}$ increases monotonically. Near the bottom wall, the flow laminarizes as θ passes through θ_c and then re-transitions to turbulence. As Re increases, θ_c increases monotonically. The transition from Couette-type to Poiseuille-type flow is accompanied by the rapid attenuation of streamwise rolls observed in pure Couette flow. A subclass of flows with $Re_{\tau,b} = 0$ is investigated. Combined WMLES with modelling for these flows enables exploration of the $Re \to \infty$ limit, giving $\theta_c \to 45°$ as $Re \to \infty$.

Key words: turbulence modelling, turbulence simulation

† Email address for correspondence: wancheng@ustc.edu.cn

‡ Professor Samtaney passed away during the preparation of this paper.

© The Author(s), 2023. Published by Cambridge University Press

https://doi.org/10.1017/jfm.2022.1023 Published online by Cambridge University Press

1. Introduction

Statistically stationary, wall-bounded turbulent flow between two parallel plane walls is an idealized canonical configuration that enables study of Reynolds number effects on wall-bounded turbulent flows. The driving force is typically either a mean-flow pressure gradient, which alone results in a plane Poiseuille (PP) flow, or the viscous force induced by moving walls which generates a plane Couette (PC) flow. For PP flow, direct numerical simulations (DNS), which resolve the smallest dissipation scale for turbulence, have been performed at $Re_\tau = 5200$ (Lee & Moser 2015) with Re_τ based on the wall skin-friction velocity. Experimental results at $Re_\tau \sim 5900$ (Schultz & Flack 2013) are available. DNS of PC flow by Pirozzoli, Bernardini & Orlandi (2014) reach $Re_\tau = 986$, while DNS of Lee & Moser (2018) – who used a larger streamwise domain – at $Re_\tau \approx 220$ showed the presence of streamwise-oriented coherent roll structures. Large-eddy simulations (LES) of PC flow (Cheng, Pullin & Samtaney 2022) up to $Re_\tau = 2.85 \times 10^5$ show the tendency of roll structures to weaken with increasing Reynolds number. Reynolds numbers achieved in experimental studies of Couette flow remain relatively low at around the onset of turbulence transition (Bottin *et al.* 1998; Couliou & Monchaux 2015) or slightly above the transition state (Tillmark & Alfredsson 1992).

The flow produced by the combination of relative moving walls and the application of a pressure gradient, here denoted as plane Couette–Poiseuille (PCP) flow, is a more complex wall-bounded flow with distinct and competing flow-driving mechanisms resulting in possibly different flow states. Generally, statistically stationary PCP flow can be characterized in a space of three parameters consisting of two independent Reynolds numbers and a single angle ϕ between the moving-plates-velocity-difference vector and the externally applied pressure-gradient vector. All possible PCP flows are contained in $0 \leq \phi \leq 90^\circ$. We will refer to $\phi = 0$ as parallel PCP flow. Pirozzoli, Bernardini & Orlandi (2011) studied PCP flow with $\phi = 0$ using DNS at bulk flow Reynolds number approximately 4800, discussing a nonlinear mechanism where a low-wavenumber flow component modulates the high-wavenumber turbulence. Gandía-Barberá *et al.* (2018) investigated PCP flow using a long streamwise domain at $Re_\tau \approx 125$, observing similar large-scale streamwise structures of length $\sim 50h$ as found in pure Couette flow by Lee & Moser (2018). Kim *et al.* (2020) and Kim & Lee (2018) utilize DNS of a temporal transition from pure PP to PCP flow to study the formation of large- and very-large-scale streamwise eddy structures. On the theoretical side, Wei, Fife & Klewicki (2007) applied a multiscale analytical approach to the mean momentum equation to estimate wall-normal positions of maxima in the Reynolds shear-stress profile in addition to proposing an intermediate or mesoscale basis for the profile shapes near those locations. Andreolli, Quadrio & Gatti (2021) investigated the turbulent characteristics of PCP flows under the constraint of constant power input.

A specifically interesting limit for PCP flow occurs when the balance between the pressure gradient and the shear provided by the wall velocity difference gives zero mean skin friction on one wall, in the sense of a time-planar average. Using DNS at a top wall, $Re_{\tau,t} \sim 180$, Yang, Zhao & Andersson (2017) report negligible turbulent energy production near the zero-stress wall, while at $Re_{\tau,t} \sim 260$, Choi, Lee & Hwang (2021) find an elongated log region in comparison to PP flow at a similar Reynolds number. Coleman *et al.* (2017) explored this state with DNS at Reynolds numbers based on the wall difference velocity up to 1.2×10^4. Using a velocity scale based on the cube root of the product of the kinematic viscosity and pressure gradient divided by fluid density, their DNS find some support for the Stratford (1959) square-root law for the variation of

https://doi.org/10.1017/jfm.2022.1023 Published online by Cambridge University Press

the streamwise velocity near the zero-shear-stress wall, over a very small region in the wall-normal dimensionless variable y^-.

Experimental studies of PCP flow have been challenging. Eltelbany & Reynolds (1980, 1981) documented measurements with a flow development distance of only $40h$ (where h is the half-channel height) at their highest Reynolds number. Interaction between the two wall layers over a long channel length of $180h$ was investigated by Thurlow & Klewicki (2000) at Re_τ up to 280. The shear Reynolds number, at approximately 10 % of the bulk Reynolds number, indicates Poiseuille- or pressure-gradient-type flow. Nakabayashi, Kitoh & Katoh (2004) studied the effect of shear-stress gradient on wall-normal velocity profiles and turbulence intensities with Re_τ up to 600, while Klotz *et al.* (2017) focused on PCP flows with zero mean advection velocity in a reference frame where one wall is stationary. In a reference frame with equal and opposite wall velocities $\pm U_c$, this corresponds to an average streamwise flow speed equal to U_c.

Turbulence behaviour of wall-bounded flows, including PCP flows, at extreme Reynolds numbers is of general interest in both research and industrial application settings. High-Reynolds-number asymptotic behaviour has been discussed by Nagib, Chauhan & Monkewitz (2007) and Pullin, Inoue & Saito (2013). A universal velocity profile for pipe flow was proposed by Cantwell (2019). The $Re \to \infty$ limit is a mean velocity plug flow. This limit is presently of interest for PCP flow. Subrahmanyam, Cantwell & Alonso (2022) extended this profile analysis to boundary layers both with and without pressure gradients.

The present work aims to provide a systematic study of some aspects of statistically stationary PCP flow using DNS, wall-resolved LES (WRLES), wall-modelled LES (WMLES) and empirical mean-flow modelling. In § 2, we define PCP flow in terms of two independent Reynolds numbers for the special case $\phi = 0$, and also define the main dependent parameters of interest. The numerical method and LES models, including the subgrid scale (SGS) model and the wall model, are also briefly discussed. Simulations performed with DNS, WRLES and WMLES are summarized in § 2.3. General features and properties of PCP flows are discussed in § 3. Section 4 describes mean-flow modelling in both the plane Couette- and Poiseuille-type domains, leading to predictions for the mean-flow velocity profiles and the mean skin-friction variation on both walls as functions of the defining flow Reynolds numbers. In § 5, we describe the general behaviour of PCP flow across the range of (Re, θ) covered by DNS and WRLES, with emphasis on the comparison between numerical results and the modelling. The transition from Couette- to Poiseuille-type flow is discussed in § 6, which includes some elements of instantaneous flow visualization, while in § 7, attention is focused on PCP flows for which the skin friction on the lower wall is zero. Concluding remarks and a summary of the work done are provided in § 8.

2. Flow description, numerical method and physical models

2.1. *Description of PCP flow*

We consider only the special case for PCP flow where the velocity-difference vector is aligned with the externally applied pressure gradient. In Cartesian coordinates (x, y, z) with y wall-normal, x streamwise and z spanwise, the parallel plane walls are at $y = \pm h$. The flow configuration is shown in figure 1, where the lower/upper walls move in the x-direction with speeds U_c and $-U_c$, respectively. The pressure-gradient vector points in the negative x-direction, so the mass-flow rate is positive. This configuration contains all possible PCP flows with $\phi = 0$. To illustrate general flow behaviour, three sketched

https://doi.org/10.1017/jfm.2022.1023 Published online by Cambridge University Press

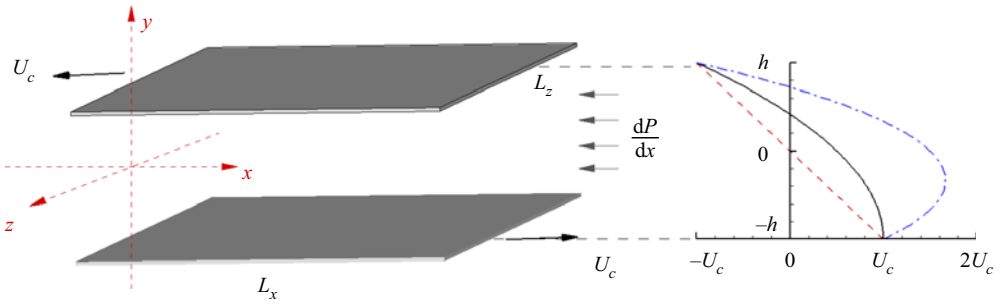

Figure 1. Sketch of PCP flow showing two parallel walls with separation distance $L_y = 2h$. Lower and upper walls move with velocities $\pm U_c$, respectively. Negative mean pressure gradient $\mathrm{d}P/\mathrm{d}x$ results in a mean bulk flow with positive mass-flow rate in the x-direction. Sketched velocity profiles: dashed line for laminar Couette flow, solid line for flow with zero skin friction on bottom wall, and dash-dotted line for flow with stronger pressure gradient.

velocity profiles are shown. The dashed line denotes a laminar Couette flow with zero pressure gradient, the solid line profile shows zero skin friction (ZSF) on the bottom wall, and the dash-dotted line represents a Poiseuille-type flow with a stronger pressure gradient.

The flow is assumed to be statistically stationary with bulk wall-parallel mean velocity $M/(2h)$, where $M > 0$ is the volume flow rate. Two independent Reynolds numbers can then be defined as

$$Re_c = \frac{U_c h}{\nu}, \quad Re_M = \frac{M}{2\nu} = \frac{1}{2\nu}\int_{-h}^{h} U(y)\,\mathrm{d}y, \tag{2.1a,b}$$

where ν is the kinematic viscosity, and $U(y)$ is the streamwise mean velocity. It is convenient to work in polar coordinates (Re, θ) defined by $Re_c = Re\cos\theta$, $Re_M = Re\sin\theta$, so that

$$Re = \sqrt{Re_c^2 + Re_M^2}, \quad \tan\theta = \frac{Re_M}{Re_c}, \tag{2.2a,b}$$

where Re is the defining Reynolds number. The PC and PP limits correspond to $\theta = 0^\circ$, $\theta = 90^\circ$, respectively. If we write $Re = U_0 h/\nu$, then this defines an effective general outer velocity scale $U_0 = U_c/\cos\theta = M/(2h\sin\theta)$ for PCP flow. The nominal singularity $U_c/\cos\theta$ as $\theta \to 90^\circ$ and $M/(2h\sin\theta)$ as $\theta \to 0^\circ$ is noted, but this does not compromise the utility of U_0 as an outer velocity over the range $\theta \in [0^\circ, 90^\circ]$.

A specific flow is defined by given Re and θ. Skin-friction velocities for both walls are defined as

$$u_{\tau,t} = \sqrt{\nu\,|\eta_h|}\,\mathrm{sgn}(-\eta_h), \quad u_{\tau,b} = \sqrt{\nu\,|\eta_{-h}|}\,\mathrm{sgn}(\eta_{-h}), \tag{2.3a,b}$$

with $\eta_y = \mathrm{d}U/\mathrm{d}y|_y$ as the velocity gradient at y. Corresponding skin-friction Reynolds numbers are

$$Re_{\tau,t} = \frac{u_{\tau,t} h}{\nu}, \quad Re_{\tau,b} = \frac{u_{\tau,b} h}{\nu}. \tag{2.4a,b}$$

With these definitions, $Re_{\tau,t} > 0$ for all PCP flows, while $Re_{\tau,b} < 0$ for PC flow ($\theta = 0^\circ$) and $Re_{\tau,b} > 0$ ($\theta = 90^\circ$) for PP flow. Hence when θ increases in $(0^\circ, 90^\circ)$ at fixed Re, $Re_{\tau,b}$ must change sign at least once. We define flow regions in the first quadrant of the (Re_c, Re_M) plane as Couette-type for $Re_{\tau,b} < 0$ and Poiseuille-type for $Re_{\tau,b} > 0$.

https://doi.org/10.1017/jfm.2022.1023 Published online by Cambridge University Press

The curve $Re_{\tau,b}(Re, \theta) = 0$ corresponds to $\theta = \theta_c$. We refer to θ_c as the $PC \leftrightarrow PP$ critical angle. This will be seen later to be a single-valued function $\theta_c(Re)$.

Another Reynolds number based on pressure gradient can also be defined as $Re_p = (-(\mathrm{d}P/\mathrm{d}x)h^3)^{1/2}/\nu$, where $P \equiv p/\rho$, with p the pressure and ρ the constant fluid density. Using the streamwise pressure–skin-friction balance, this can be expressed as

$$Re_p^2 = \tfrac{1}{2}(Re_{\tau,t}|Re_{\tau,t}| + Re_{\tau,b}|Re_{\tau,b}|). \tag{2.5}$$

Since, as will be seen, $Re_{\tau,t}$ and $Re_{\tau,b}$ are both functions of (Re, θ) only, Re_p is also a function of (Re, θ).

2.2. *Numerical methods and LES models*

Simulations are reported using an incompressible Navier–Stokes solver for a channel domain with dimensions $L_x \times L_y \times L_s$ (streamwise, wall-normal and spanwise directions, respectively). Boundary conditions are spatially periodic streamwise and spanwise, with Dirichlet velocity boundary conditions on $y = \pm h$. Both DNS and LES are performed. The generically filtered incompressible Navier–Stokes equations are

$$\frac{\partial \widetilde{u}_i}{\partial t} + \frac{\partial \widetilde{u}_i \widetilde{u}_j}{\partial x_j} = -\frac{\partial \widetilde{P}}{\partial x_i} + \nu \frac{\partial^2 \widetilde{u}_i}{\partial x_j^2} - \frac{\partial T_{ij}}{\partial x_j}, \quad \frac{\partial \widetilde{u}_i}{\partial x_i} = 0, \tag{2.6}$$

$$\tilde{q} = \int_{-\infty}^{\infty} q(x')\, G(x - x')\, \mathrm{d}x', \tag{2.7}$$

where $G(\eta)$ is a general filter. Boundary conditions are

$$\widetilde{u}_i = (U_c + u_b, v_b, w_b), \quad \text{at the bottom wall,} \tag{2.8}$$

$$\widetilde{u}_i = (-U_c + u_t, v_t, w_t), \quad \text{at the upper wall.} \tag{2.9}$$

The DNS mode uses the unfiltered Navier–Stokes equations, while LES requires modelling for the SGS tensor $T_{ij} = \widetilde{u_i u_j} - \widetilde{u}_i \widetilde{u}_j$ with the added assumption that filtered fields are identified with computed resolved-scale fields. Explicit filtering is used nowhere presently. For DNS and WRLES, (u_b, v_b, w_b) and (u_t, v_t, w_t) are zero, while for WMLES, a wall model provides consistent slip velocity boundary conditions at a virtual wall. The fractional-step method is used to solve the equations with a third-order Runge–Kutta method for temporal evolution. The staggered grid strategy ensures the conservation of kinetic energy, which corresponds to a skew-symmetric form of the convective term. The pressure Poisson equation is reduced to a series of one-dimensional linear equations by Fourier expansion in the streamwise and spanwise directions. In simulations, the time step Δt satisfies dynamically that a Courant–Friedrichs–Lewy number be unity.

For LES, T_{ij} is evaluated using the stretched-vortex SGS model, which represents subgrid motion using stretched vortices in each computational cell (Chung & Pullin 2009), with directional unit vector $\boldsymbol{e}^v$ aligned with the principal extensional rate-of-strain eigenvector of the local resolved flow, giving

$$T_{ij} = (\delta_{ij} - e_i^v e_j^v)K, \quad K = \int_{k_c}^{\infty} E(k)\, \mathrm{d}k, \tag{2.10a,b}$$

where K is the subgrid kinetic energy, and $E(\kappa)$ is the SGS energy spectrum. Closure of $E(k)$ uses the stretched-spiral vortex solution of the Navier–Stokes equation (Lundgren 1982). See Chung & Pullin (2009).

https://doi.org/10.1017/jfm.2022.1023 Published online by Cambridge University Press

For WMLES, the virtual-wall model (VWM) is used (Chung & Pullin 2009). This consists first of an ordinary differential equation for $u_\tau(x, z, t)$ at each wall point, derived from an integration in the wall-normal direction of the local streamwise momentum equation over a thin wall-adjacent layer $0 \le y \le \delta$ and given by

$$\frac{\mathrm{d}u_\tau}{\mathrm{d}t} = \frac{u_\tau}{\tilde{u}|_\delta}\left(-\frac{\partial \widetilde{uu}}{\partial x}\bigg|_\delta - \frac{\partial \widetilde{uw}}{\partial z}\bigg|_\delta - \frac{\partial \tilde{P}}{\partial x}\bigg|_\delta - \frac{1}{\delta}\,\widetilde{uv}|_\delta + \frac{\nu}{\delta}\,\frac{\partial \tilde{u}}{\partial y}\bigg|_\delta - \frac{1}{\delta}\,u_\tau^2\right). \tag{2.11}$$

With $u_\tau(x, y, t)$ known, the VWM then provides a slip-velocity boundary condition at a virtual wall of $y = \delta_0 < \delta$ as

$$\tilde{u}(\delta_0^+) = u_\tau\left(\frac{1}{\kappa}\ln\left(\frac{\delta_0^+}{\delta_\nu^+}\right) + \delta_\nu^+\right), \tag{2.12}$$

with $\kappa = \gamma K^{1/2} u_\tau/(-2T_{xy})$ and where δ_ν^+ is an effective offset parameter. See Chung & Pullin (2009) and Saito, Pullin & Inoue (2012) for computational details and sensitivity testing. Where at a wall u_τ is very small compared with the outer velocity scale, the VWM is turned off.

2.3. *Simulations performed*

We report two series of simulations, the first for general PCP flow, and the second focused on a subset of flows with $Re_{\tau,b} = 0$ on the bottom wall (ZSF flows). Pirozzoli *et al.* (2011) reported DNS of PCP at $Re_\tau \approx 250$ with a relatively small wall-parallel domain approximately $(L_x \times L_z) = (12\pi h \times 4\pi h)$. Pirozzoli *et al.* (2014) suggested that a domain $(L_x \times L_z) = (60h \times 16h)$ is generally required to eliminate spurious flow confinement effects, a rule generally followed in simulations by Avsarkisov *et al.* (2014), Lee & Moser (2018) and Cheng *et al.* (2022). Lee & Moser (2018) report that the spanwise domain has a non-negligible effect on some mean profile diagnostics, for example the velocity gradient at the channel centre, which shows an almost 20 % relative error at around $Re_\tau \approx 220$. The computational domain for all present simulations is chosen as $L_x \times L_y \times L_z = 20\pi h \times 2h \times 6\pi h$.

Direct numerical simulation flows include $Re = 4000$, 6000, while WRLES is implemented for $Re = 10\,000$, $20\,000$. For each Re, $\theta = 0°$, 15°, 30°, 35°, 37.5°, 40°, 42.5°, 45°, 47.5°, 50°, 60°, 75° and 90°. Simulation flow parameters are summarized in figure 2, showing both the (Re, θ) and (Re_M, Re_c) planes. For each Re, a specific mesh is employed. For DNS at $Re = 4000$ and 6000, we have $N_x \times N_y \times N_z = 2048 \times 256 \times 1024$ and $N_x \times N_y \times N_z = 3072 \times 320 \times 1536$, respectively. For WRLES at $Re = 10\,000$, we have $N_x \times N_y \times N_z = 2048 \times 128 \times 1024$, while for $Re = 20\,000$, we have $N_x \times N_y \times N_z = 3072 \times 160 \times 1536$. For both DNS and WRLES, grid-stretching in the wall-normal direction is used as described in Cheng *et al.* (2022). For WMLES, the grid is uniform in all directions. Validation studies of both WRLES and WMLES for PC flow were conducted by Cheng *et al.* (2022), who also reported on the effect of spanwise domain size on flow diagnostics at $Re_\tau = 500$.

Table 1 summarizes Re, the mesh resolution and the corresponding numerical methodology for ZSF flow simulations. Also shown are calculated values of $Re_{\tau,t}$. Values of both $Re_{\tau,t}$ and $Re_{\tau,b}$ reported presently were obtained as time-planar averages over a time window Γ_t, defined as $N_t \times \max(|u_{\tau,b}|, |u_{\tau,t}|)h/\nu$, consisting of many wall-transit times through the computational domain. Here, $N_t \approx 20$ for DNS, and $N_t \approx 50$ for

https://doi.org/10.1017/jfm.2022.1023 Published online by Cambridge University Press

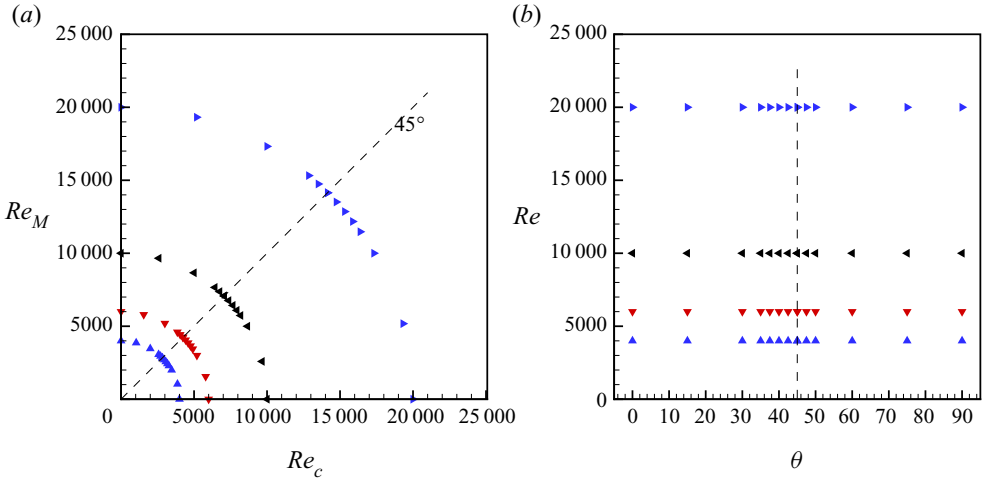

Figure 2. Parameters for general PCP flow: simulation points in (*a*) the (Re_M, Re_c) plane, (*b*) the (Re, θ) plane. Each symbol denotes a specific simulation. Here, $Re_c = U_c h/\nu$, $Re_M = M/(2\nu)$, $Re \equiv (Re_c^2 + Re_M^2)^{1/2} = U_0 h/\nu$ and $\theta = \arccos(Re_c/Re)$. Blue ▲ indicates DNS at $Re = 4000$ with mesh $2048 \times 256 \times 1024$. Red ▼ indicates DNS at $Re = 6000$ with mesh $3072 \times 320 \times 1536$. Black ◀ indicates WRLES at $Re = 10\,000$ with mesh $2048 \times 128 \times 1024$. Blue ▶ indicates WRLES at $Re = 20\,000$ with mesh $3072 \times 160 \times 1536$.

Re	N_x	N_y	N_z	Method	$Re_{\tau,t}$	θ_c
100	512	96	256	DNS	13.9	18.4
300	512	96	256	DNS	23.9	18.4
1000	768	128	384	DNS	89.8	33.5
4000	2048	256	1024	DNS	304	36.0
6000	3072	320	1536	DNS	433	36.7
10 000	2048	128	1024	WRLES	685	37.0
20 000	3072	160	1536	WRLES	1256	37.7
10^5	576	96	192	WMLES	5.42×10^3	39.9
10^6	576	96	192	WMLES	4.55×10^4	40.9
10^7	576	96	192	WMLES	3.90×10^5	41.5
10^8	576	96	192	WMLES	3.41×10^6	42.0
10^9	576	96	192	WMLES	3.03×10^7	42.4
10^{10}	576	96	192	WMLES	2.72×10^8	42.7

Table 1. Simulations for PCP flows with ZSF on the bottom wall, where Re is fixed for each simulation, with θ such that the bottom-wall frictional Reynolds number is $Re_{\tau,b} \approx 0$. The final two columns show the computed top-wall frictional Reynolds number $Re_{\tau,t}$ and the ZSF angle θ_c, respectively. The computational domain is $(L_x/h, L_y/h, L_z/h) = (18\pi, 2, 6\pi)$.

WRLES and WMLES. Several low-Re DNS cases are included in table 1, including laminar flow at $Re = 100$ and 300, and an incipient turbulent flow at $Re = 1000$. Simulations reported include $Re = 4000$ and 6000 (DNS), and $Re = 10\,000$ and $20\,000$ (WRLES). To access higher Re, WMLES were performed for $Re = 10^5$, 10^6, 10^7, 10^8, 10^9 and 10^{10}.

https://doi.org/10.1017/jfm.2022.1023 Published online by Cambridge University Press

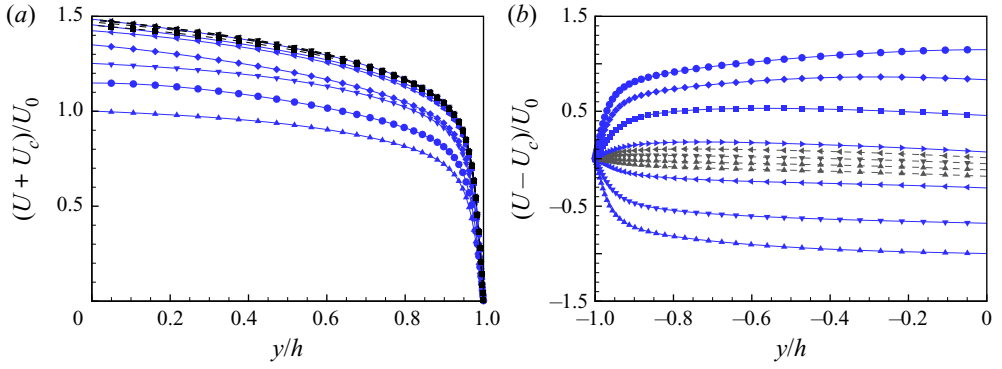

Figure 3. (*a*) Velocity $U + U_c$ in the upper-wall reference frame. (*b*) Mean velocity $U - U_c$ in the bottom-wall reference frame. Solid lines with blue symbols: ▲, $\theta = 0°$; ▼, $\theta = 15°$; ◀, $\theta = 30°$; ▶, $\theta = 45°$; ■, $\theta = 60°$; ♦, $\theta = 75°$; ●, $\theta = 90°$. Dashed lines with black symbols: ■, $\theta = 35°$; ▲, $\theta = 37.5°$; ▼, $\theta = 40°$; ◀, $\theta = 42.5°$.

3. Background features of turbulent PCP flow

We first discuss the mean streamwise velocity profiles at $Re = 6000$ in order to provide background for mean-flow modelling to be described.

3.1. *Velocity statistics at* $Re = 6000$

Figure 3 shows profiles in velocity-difference form to highlight changes in the near-wall velocity gradients as θ changes at fixed Re. Figure 3(*a*) shows $(U(y) - U_c)/U_0$ for flow near the bottom wall, while figure 3(*b*) depicts $(U + U_c)/U_0$ for flow near the upper wall. The velocity gradient on the top wall reaches a maximum at around $\theta \approx 45°$, while the bottom-wall velocity gradient changes sign at $\theta \approx 37.5°$, corresponding to $Re = 6000$. This is the general change from Couette-type to Poiseuille-type flow.

Wall-relative mean velocity profiles for the top wall in the form $U_t^+ = (U + U_c)/u_{\tau,t}$ versus $d_t^+ = (h - y)u_{\tau,t}/\nu$ are shown in figure 4(*a*) for seven values of θ. For flow near the bottom wall, plots of $U_b^+ = (U - U_c)/u_{\tau,b}$ versus $d_b^+ = (h + y)|u_{\tau,b}|/\nu$ in figure 4(*b*) show negative and positive wall-relative velocity for Couette-type and Poiseuille-type flow, respectively. The velocity gradient indicator function $\Xi(d^+)$ is shown in figure 5. Near the top wall and the bottom walls, Ξ_t and Ξ_b are defined respectively as

$$\Xi_t = d_t^+ \frac{\mathrm{d}U_t^+}{\mathrm{d}(d_t^+)}, \quad \Xi_b = d_b^+ \frac{\mathrm{d}U_b^+}{\mathrm{d}(d_b^+)}. \tag{3.1a,b}$$

In figure 5(*a*), all flows indicate the presence of a logarithmic region with $\Xi_t \approx 2.5$, with reasonable collapse over the whole range of θ in figure 4(*a*). In figure 5(*b*), nearly constant Ξ_t regions are apparent only for θ near or at $\theta = 0°$ and 90°. As θ moves between these limit values, the logarithmic-like region breaks and then rebuilds during the transition from PC flow to PP flow. This can be seen clearly in the mean profiles in figure 4(*b*).

For a model log profile of the form $U^+ = \ln(d^+)/\kappa + A$, Lee & Moser (2015) suggested $\kappa = 0.384$ and $A = 4.27$ obtained from DNS of PP flow, while Pirozzoli *et al.* (2014) found that $\kappa = 0.41$ and $A = 5$ provide a good fit for PC flow. Later DNS of PC flow by Lee & Moser (2018) found similar values. In figure 4(*b*), we use these different values for the log

https://doi.org/10.1017/jfm.2022.1023 Published online by Cambridge University Press

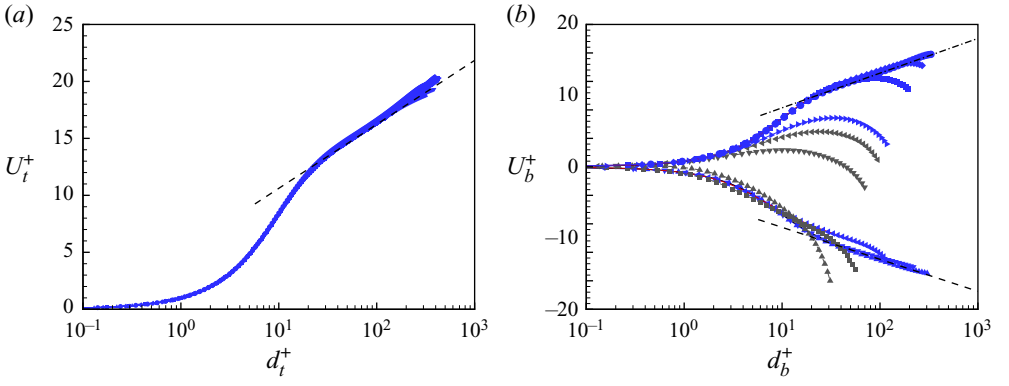

Figure 4. Mean streamwise velocity profiles at $Re = 6000$. (*a*) Scaling with the upper-wall friction velocity $u_{\tau,t}$: $U_t^+ = (U + U_c)/u_{\tau,t}$, $d_t^+ = (h - y)u_{\tau,t}/\nu$. (*b*) Scaling with the bottom-wall friction velocity $u_{\tau,b}$: $U_b^+ = (U - U_c)/u_{\tau,b}$, $d_b^+ = (h + y)|u_{\tau,b}|/\nu$. Symbols as in figure 3. Reference log law: $U^+ = \ln(d^+)/\kappa + A$. Dashed lines indicate $\kappa = 0.41$ and $A = 5.1$. Dash-dotted lines indicate $\kappa = 0.384$ and $A = 4.27$.

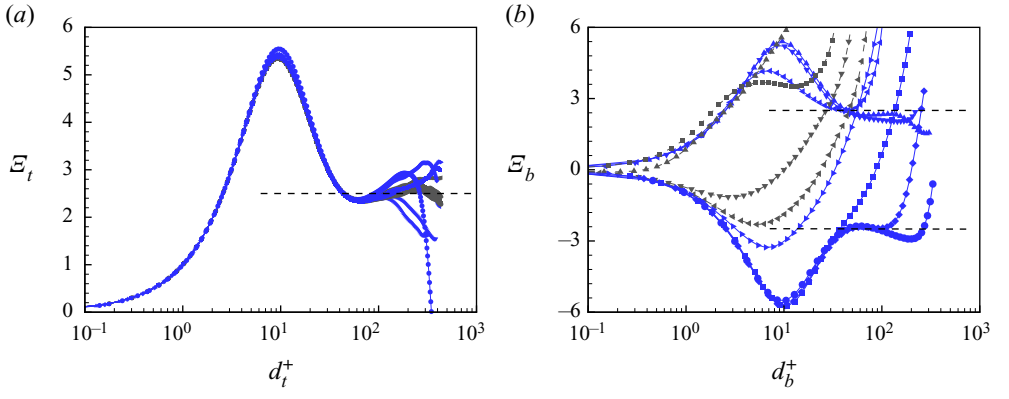

Figure 5. Scaled velocity gradient Ξ at $Re = 6000$. (*a*) Scaling with the upper-wall friction velocity $u_{\tau,t}$: $\Xi_t = d_t^+ \,\mathrm{d}(U_t^+)/\mathrm{d}(d_t^+)$. (*b*) Scaling with the bottom-wall friction velocity $u_{\tau,b}$: $\Xi_b = d_b^+ \,\mathrm{d}(U_b^+)/\mathrm{d}(d_b^+)$. Symbols as in figure 3. Reference dashed lines: $\Xi = \pm 2.5$.

lines shown in the PP and PC flow limits, respectively. In figure 4(*a*), the PC values are used.

3.2. *Turbulent kinetic energy budget at Re* = 6000

In the transition from PC flow to PP flow, the velocity deviation from the log law for some cases indicates that the flow deviates from behaviour typical of canonical wall-bounded turbulence. To evaluate the flow near the bottom wall, we investigate the turbulent kinetic energy budget. The transport equation for the turbulent kinetic energy $e = u'^2 + v'^2 + w'^2$ can be obtained by multiplying the Navier–Stokes momentum equations by u_i, subtracting the equation for the mean momentum equation, and taking a time-planar average. For statistically stationary flow, this can be expressed as

$$P + T + \Pi + D + \epsilon = 0, \tag{3.2}$$

https://doi.org/10.1017/jfm.2022.1023 Published online by Cambridge University Press

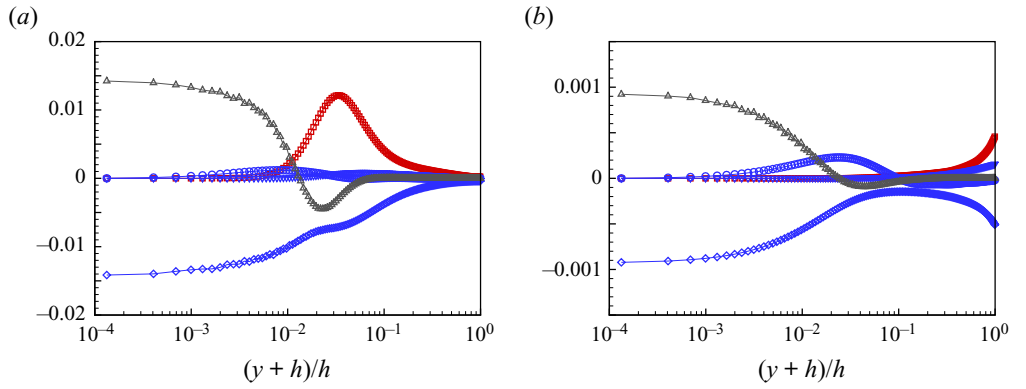

Figure 6. Turbulent kinetic energy budget near the bottom wall for $Re = 6000$: (*a*) $\theta = 0^\circ$, pure Couette flow; (*b*) $\theta = 37.5^\circ$, with small skin-friction magnitude on the bottom wall. Red $\square$, P turbulence production; blue $\circ$, Π pressure transport; blue $\triangledown$, T turbulent transport; black $\triangle$, D diffusion; blue $\diamond$, ϵ dissipation.

with P, T, Π, D and ϵ denoting the turbulent production, turbulent transport, pressure transport, viscous diffusion and dissipation terms, respectively. These are given by

$$\left.\begin{aligned} P(y) &\equiv -\overline{u'v'}\,\frac{\mathrm{d}U}{\mathrm{d}y}, \quad T(y) \equiv -\frac{\mathrm{d}\overline{(ev')}}{\mathrm{d}y}, \quad \Pi(y) \equiv -\frac{\mathrm{d}\overline{(pv'/\rho)}}{\mathrm{d}y}, \\ D(y) &\equiv \nu\,\frac{\mathrm{d}^2\bar{e}}{\mathrm{d}y^2}, \quad \epsilon(y) \equiv -\nu\,\overline{\left(\frac{\partial u_i}{\partial x_j}\right)^2}, \end{aligned}\right\} \tag{3.3}$$

with the overbar referring to a plane and time average to be defined explicitly later, in (5.1*a*,*b*).

Figures 6(*a*,*b*), respectively, show profiles of these terms over the bottom half-channel for two cases: pure Couette flow $\theta = 0^\circ$ and also $\theta = 37.5^\circ$, where the bottom-wall skin friction is almost zero. All are normalized on outer scales as $U_c^3 h^{-1}$. Pure Couette flow displays the well-known near-wall balance of diffusion with dissipation, changing to an inertial-range balance between turbulent production and dissipation at larger wall-normal distances. For $\theta = 37.5^\circ$, all terms are reduced by an order of magnitude. A diffusion–dissipation balance is again present in the near-bottom-wall flow, while farther out, the production almost vanishes. Flow with $\theta = 0^\circ$ shows a generally similar balance profile to the corresponding case reported by Pirozzoli *et al.* (2011), while our flow with $\theta = 37.5^\circ$ shows smaller production near the centreline than that of their SL (shearless) flow.

Figure 7 shows wall-normal profiles of the production–dissipation ratio P/ϵ at $Re = 6000$. In figure 7(*a*), with θ from 0° to 42.5°, all profiles collapse near the upper wall. Away from this wall, there is rapid increase to approximately $P/\epsilon \approx 2$, with further decrease to $P/\epsilon \sim 1$ in the inertial region. Near the bottom wall, the peak value decreases monotonically with increasing θ. For $\theta = 37.5^\circ$, no obvious peaks are found, with P/ϵ increasing slowly with distance from the bottom wall. Further increasing θ gives negative P/ϵ, so that production becomes negative in the near-bottom-wall region. At $\theta = 42.5^\circ$, P/ϵ again becomes positive close to the bottom wall.

The appearance of negative P/ϵ over $37.5^\circ \lesssim \theta \lesssim 45^\circ$ generally represents energy transfer from unsteady fluctuations to the mean flow. This implies that the kinetic energy of the fluctuating (unsteady) flow is suppressed, and that the near-wall flow has

https://doi.org/10.1017/jfm.2022.1023 Published online by Cambridge University Press

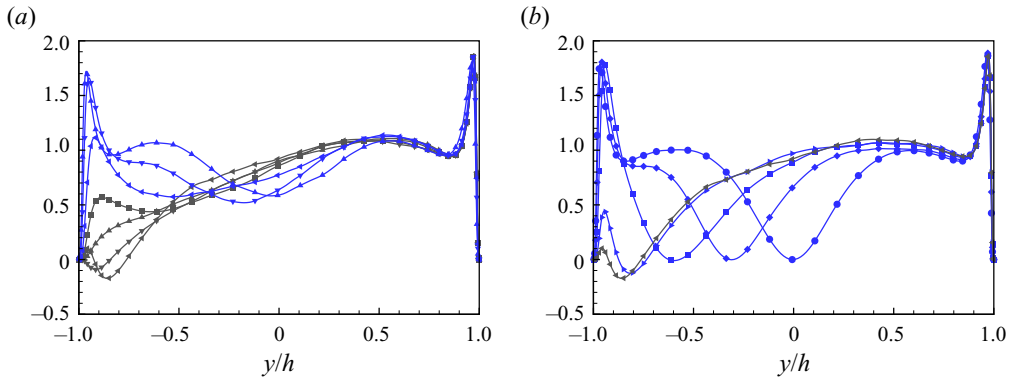

Figure 7. Distribution of the ratio of turbulent production and dissipation for $Re = 6000$. Each line corresponds to a different θ. (*a*) Blue symbols: ▲, $\theta = 0°$; ▼, $\theta = 15°$; ◀, $\theta = 30°$. Black symbols: ■, $\theta = 35°$; ▲, $\theta = 37.5°$; ▼, $\theta = 40°$; ◀, $\theta = 42.5°$. (*b*) Black symbol: ◀, $\theta = 42.5°$. Blue symbols: ▶, $\theta = 45°$; ■, $\theta = 60°$; ♦, $\theta = 75°$; ●, $\theta = 90°$.

effectively laminarized. Negative P/ϵ first appears across the ZSF boundary (see § 7 for more discussion) near $\theta = 37.5°$, where $\mathrm{d}U/\mathrm{d}y$ changes sign, while $\overline{u'v'}$ remains small but negative. At around $\theta \approx 42.5°$, $\overline{u'v'}$ changes sign in the near-bottom-wall flow, which regenerates positive production, although the corresponding peak value of P/ϵ remains small.

Figure 7(*b*) shows P/ϵ profiles in the range $42.5° \leq \theta \leq 90°$. For these flows, the regenerated peak value increases from near zero to $P/\epsilon \approx 2$ at $\theta = 60°$. Further increase in θ leads to the re-establishment of production–dissipation balance as the near-bottom-wall flow re-transitions to a classical wall-bounded turbulent state.

3.3. *Mean velocity profile near ZSF on the bottom wall*

Averaging and wall-normal integration of the streamwise momentum equation in $(-h, y)$ gives the relation between the stress $\overline{u'v'}(y)$ and the mean velocity gradient as

$$\overline{u'v'}(y) - \nu \left.\frac{\partial \bar{u}}{\partial y}\right|_y = -S\,u_{\tau,b}^2 - \frac{\mathrm{d}P}{\mathrm{d}x}(y+h), \quad S = \mathrm{sgn}\left(\left.\frac{\mathrm{d}U(y)}{\mathrm{d}y}\right|_{-h}\right), \qquad (3.4a,b)$$

where $S = -1$ for Couette-type flows, and $S = 1$ for Poiseuille-type flows. In obtaining (3.4*a*,*b*), possible non-homogeneity in the spanwise direction is ignored. This is not important presently, and will be discussed later. In figure 8, we plot the distribution of the Reynolds stress $\overline{u'v'}$. Figure 8(*a*) shows $\overline{u'v'}/u_{\tau,t}^2$ for all θ at $Re = 6000$ using top-wall inner scaling, while figure 8(*b*) shows $\overline{u'v'}/u_{\tau,b}^2$ using bottom-wall inner scaling, for flows near $u_{\tau,b} = 0$. In figure 8(*a*), the stress distribution near the top wall shows a collapse in inner scaling, while near but not very close to the bottom wall, the stress distribution shows a consistent tendency of decreasing magnitude, from a plateau of $\overline{u'v'}/u_{\tau,t}^2 \approx 1$ for $\theta = 0°$, to almost zero for $\theta \approx 40°$, with further decrease to $\overline{u'v'}/u_{\tau,t}^2 \approx -1$ for $\theta = 90°$. This tendency is similar to the distribution of $\overline{u'v'}/U_0^2$, which is not shown presently. Near the ZSF condition, there is no observable collapse for $\overline{u'v'}/u_{\tau,t}^2$. In figure 8(*b*), the Reynolds stress is plotted using bottom-wall inner scaling, showing large scatter.

https://doi.org/10.1017/jfm.2022.1023 Published online by Cambridge University Press

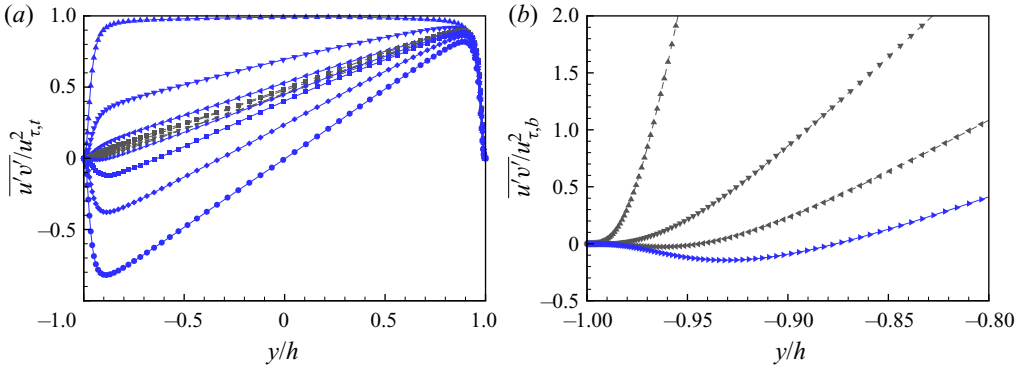

Figure 8. Profile of Reynolds stress $\overline{u'v'}$ versus y/h for $Re = 6000$: (*a*) $\overline{u'v'}/u_{\tau,t}^2$ for all θ flows; (*b*) $\overline{u'v'}/u_{\tau,b}^2$ for simulations near the ZSF flow. Symbols as in figure 3.

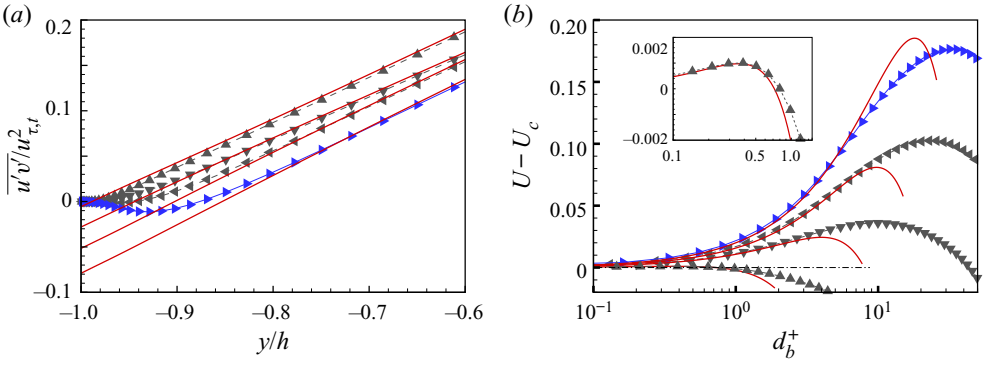

Figure 9. Balance of wall-normal integral of the streamwise momentum equation. (*a*) Equation (3.4*a*,*b*). Symbols: close-up of $\overline{u'v'}/u_{\tau,t}^2$ for near-ZSF flows. Solid lines: $(-u_{\tau,b}^2 - (\mathrm{d}P/\mathrm{d}x)(y+h))/u_{\tau,t}^2$ for corresponding θ. (*b*) Balance of (3.6). Symbols: simulation $U - U_c$ for near-ZSF flows. Solid lines: $(1/\nu)(S\,u_{\tau,b}^2(y+h) - ((u_{\tau,t}^2 + S\,u_{\tau,b}^2)/4h)(y+h)^2)$ for corresponding θ. Black symbols: ▲, $\theta = 37.5°$; ▼, $\theta = 40°$; ◀, $\theta = 42.5°$. Blue symbol: ▶, $\theta = 45°$.

A near-wall close-up of figure 8(*a*) is shown in figure 9(*a*) for $\theta = 40°, 42.5°, 45°$ near but above the ZSF condition. Solid lines are the scaled right-hand side of (3.4*a*,*b*) as $(-S\,u_{\tau,b}^2 - (\mathrm{d}P/\mathrm{d}x)(y+h))/u_{\tau,t}^2$. Up to some distance from the bottom wall, the velocity gradient term and the pressure term contribute strongly to the balance of (3.4*a*,*b*).

Further integration of the streamwise momentum equation in $(-h, h)$ and elimination of $\mathrm{d}P/\mathrm{d}x$ from (3.4*a*,*b*) gives

$$\overline{u'v'}(y) - \nu\left.\frac{\partial \bar{u}}{\partial y}\right|_y = \frac{h+y}{2h}\left(u_{\tau,t}^2 + S\,u_{\tau,b}^2\right) - S\,u_{\tau,b}^2. \tag{3.5}$$

Integration of (3.5) in $(-h, y)$ then leads to an expression for the mean velocity profile as

$$U(y) - U_c = \frac{1}{\nu}\left(S\,u_{\tau,b}^2(y+h) - \frac{u_{\tau,t}^2 + S\,u_{\tau,b}^2}{4h}(y+h)^2 + \int_{-h}^{y}\overline{u'v'}(\xi)\,\mathrm{d}\xi\right). \tag{3.6}$$

Figure 9(*b*) shows the velocity profiles near the bottom wall for three cases, $\theta = 40°,\ 42.5°, 45°$, which, from figure 8, have $Re_{\tau,b} > 0$. Equation (3.6) is also plotted

https://doi.org/10.1017/jfm.2022.1023 Published online by Cambridge University Press

using $u_{\tau,t}$ and $u_{\tau,b}$ from the simulations but with $\overline{u'v'} \equiv 0$. This shows a qualitatively similar shape to simulation profiles: a near-wall peak is indicated with increasing maximum and with location that moves off from the wall with increasing θ at fixed $Re = 6000$.

In summary, with Re fixed and sufficiently large for Poiseuille/Couette flow turbulence to exist, the flow near the top wall remains in a turbulent state while θ increases in $0^\circ \leq \theta \leq 90^\circ$. Near the bottom wall, the turbulence gradually weakens as θ is increased. Both production and dissipation reduce, with production becoming negative over a small range $37.5^\circ \lesssim \theta \lesssim 42.5^\circ$. Taken together with the loss of a log-like region, this indicates that the near-bottom-wall flow has laminarized perhaps over a range $\theta \approx 30^\circ - 50^\circ$. Further increase in θ re-establishes near-bottom-wall turbulence up to the Poiseuille limit $\theta = 90^\circ$. During flow laminarization, the pressure gradient effect is small for $\theta < \theta_c$, while it produces a near-wall mean velocity maximum with almost laminar flow between the maximum and the wall for $\theta > \theta_c$. Shear stresses on both walls contribute to the form of this profile. The general profile shape indicates laminar flow near the bottom wall for small $\theta - \theta_c > 0$.

4. Mean-flow modelling

The friction Reynolds numbers $Re_{\tau,t}$ and $Re_{\tau,b}$ defined by (2.4*a*,*b*) take the sign of the frictional force exerted on the walls by the fluid. For pure Couette flow with $\theta = 0^\circ$, $Re_{\tau,t} > 0$ and $Re_{\tau,b} < 0$, while for pure Poiseuille flow with $\theta = 90^\circ$, both $Re_{\tau,t}$ and $Re_{\tau,b}$ are positive. We expect $Re_{\tau,t} = f_t(Re, \theta)$ and $Re_{\tau,b} = f_b(Re, \theta)$. Here, we show that relatively simple, empirically based mean-flow modelling enables approximate determination of these functions. Three different models are developed for three different flow regimes. The first model, denoted CT, is for Couette-type flow with $Re_{\tau,b} < 0$. The second is PT-I for strongly Poiseuille-type flow. These are considered high-Re approximations. The third model is denoted PT-II for weakly Poiseuille-type flow, with $Re_{\tau,b} > 0$ but sufficiently small in magnitude that the flow near the bottom wall can be modelled as laminar flow as indicated by earlier discussion. The three models use the same approach, so quantitative details are given here only for the CT model. The models employ log profiles. In numerical calculations, the possible distinctions between PP and PC flows are ignored, and the nominal values $\kappa = 0.4$ and $A = 5.0$ are utilized.

4.1. *CT: Couette-type flow, $Re_{\tau,b} < 0$*

For Couette-type flow, we assume that the composite mean velocity profile comprises two pure log profiles (relative to the top and bottom walls) that join at a location $y = y_0$ to be determined.

For $-h < y \leq y_0$,

$$U_b(y) = U_c + u_{\tau,b}\left(\frac{1}{\kappa}\ln\left(\frac{(h+y)\,|u_{\tau,b}|}{\nu}\right) + A\right). \tag{4.1}$$

For $y_0 \leq y < h$,

$$U_t(y) = -U_c + u_{\tau,t}\left(\frac{1}{\kappa}\ln\left(\frac{(h-y)u_{\tau,t}}{\nu}\right) + A\right), \tag{4.2}$$

https://doi.org/10.1017/jfm.2022.1023 Published online by Cambridge University Press

where κ is the Kármán parameter, and A is the offset constant. For $\theta < \theta_c$ but $\theta - \theta_c$ small, the profiles are not accurate. But because this is a high- Re model, it is expected to have a small effect, which is verified in what follows.

When expressed in terms of Reynolds numbers, with Re, θ given, there are three unknowns, $Re_{\tau,b}$, $Re_{\tau,t}$ and y_0/h. Two equations are obtained from matching $U(y)$ and $\mathrm{d}U/\mathrm{d}y$ at $y = y_0$ using the above profiles:

$$U_b(y_0) = U_t(y_0), \qquad \left.\frac{\mathrm{d}U_b}{\mathrm{d}y}\right|_{y_0} = \left.\frac{\mathrm{d}U_t}{\mathrm{d}y}\right|_{y_0}. \tag{4.3a,b}$$

Using (4.1) and (4.2), these give, respectively, after some algebra,

$$2\kappa\, Re\cos(\theta) - A\kappa\left(Re_{\tau,t} - Re_{\tau,b}\right) + Re_{\tau,b}\ln\left(|Re_{\tau,b}|\,(1+Y_0)\right) - Re_{\tau,t}\ln\left(Re_{\tau,t}(1+Y_0)\right) = 0, \tag{4.4}$$

$$Y_0 = -\frac{Re_{\tau,t} + Re_{\tau,b}}{Re_{\tau,t} - Re_{\tau,b}}, \tag{4.5}$$

where $Y_0 = y_0/h$. A third equation is obtained by substituting (4.1) and (4.2) into the second equation of (2.1a,b) to give

$$Re_M \equiv Re\sin\theta = \frac{1}{2\nu}\left[\int_{-h}^{y_0} U_b(y)\,\mathrm{d}y + \int_{y_0}^{h} U_t(y)\,\mathrm{d}y\right]. \tag{4.6}$$

The integrations can be done, and the resulting equation, with Re and θ given, is

$$\begin{aligned} &Re_{\tau,t} + Re_{\tau,b} - Y_0\left(Re_{\tau,t} - Re_{\tau,b}\right) \\ &\quad + \kappa\left[2\,Re\sin(\theta) - 2Y_0\,Re\cos(\theta) + A\left(-Re_{\tau,t} - Re_{\tau,b} + Y_0\left(Re_{\tau,t} - Re_{\tau,b}\right)\right)\right] \\ &\quad - (1+Y_0)\,Re_{\tau,b}\,\ln\left[|Re_{\tau,b}|\,(1+Y_0)\right] - (Y_0 - 1)\,Re_{\tau,t}\ln\left[Re_{\tau,t}(1-Y_0)\right] = 0. \end{aligned} \tag{4.7}$$

Equations (4.4), (4.5) and (4.7) describe Couette-type flow with $Re_{\tau,b} < 0$. Near-wall viscous sublayer regions can be included at the cost of additional complexity, but the effect is negligibly small at values of Re presently considered, even for near-bottom-wall flow when $|Re_{\tau,b}|$ is small.

For $\theta = 0^\circ$, these equations have the exact solution $Re_{\tau,b} = -Re_{\tau,t}$, $Y_0 = 0$ and

$$Re_{\tau,t} = \frac{\kappa\, Re}{W(\mathrm{e}^{A\kappa}\,\kappa\, Re)}, \tag{4.8}$$

corresponding to pure Couette flow, where $W(Z)$ is the ProductLog function or Lambert function, which is the solution of $Z = W\ln(W)$. For given Re and $\theta > 0$, they must generally be solved numerically, which is straightforward. Their validity extends to $Re_{\tau,b} = 0$, $\theta = \theta_c$, which is the limit of Couette-type flow. Putting $Re_{\tau,b} = 0$, $Y_0 = -1$ leads to a considerable simplification. The resulting equations can be solved approximately by putting $\theta_c = \pi/4 + \epsilon$, $\epsilon \ll 1$. Linearizing in ϵ and solving the resulting equations gives

$$Re_{\tau,t}(Re) = \frac{\sqrt{2}\,\kappa\, Re}{W(2\sqrt{2}\,\mathrm{e}^{A\kappa-1}\,\kappa\, Re)}, \tag{4.9}$$

$$\theta_c(Re) = \frac{\pi}{4} - \frac{1}{W(2\sqrt{2}\,\mathrm{e}^{A\kappa-1}\,\kappa\, Re)} + HOT, \tag{4.10}$$

with HOT representing 'higher-order terms'. As $Re \to \infty$, $\theta_c \to \pi/4 = 45^\circ$. A physical interpretation of this limit will be discussed later.

https://doi.org/10.1017/jfm.2022.1023 Published online by Cambridge University Press

4.2. *PT-I: strongly Poiseuille-type flow, $Re_{\tau,b} \gg 0$*

For strongly Poiseuille-type flow with $Re_{\tau,b} > 0$, owing to the expected maximum in $U(y)$, we employ a modelling ansatz with different features to that used for $Re_{\tau,b} < 0$. In place of pure log profiles, we use the log-wake profile of Jones, Marusic & Perry (2001), which takes the form

$$\frac{U}{u_\tau} = \frac{1}{\kappa}\ln\left(\frac{yu_\tau}{\nu}\right) + A - \frac{1}{3\kappa}\left(\frac{y}{h}\right)^3 + 2\frac{\Pi}{\kappa}\left(\frac{y}{h}\right)^2\left(3 - 2\left(\frac{y}{h}\right)\right), \tag{4.11}$$

where Π is the Coles wake parameter. This profile automatically has zero slope at $y = h$. For Poiseuille-type flow, (4.11) is adapted as follows.

For $-h < y \le y_0$,

$$U_b(y) = U_c + u_{\tau,b}\left[\frac{1}{\kappa}\ln\left(\frac{(y+h)u_{\tau,b}}{\nu}\right) + A - \frac{1}{3\kappa}\left(\frac{y+h}{y_0+h}\right)^3 + 2\frac{\Pi}{\kappa}\left(\frac{y+h}{y_0+h}\right)^2\left(3 - 2\frac{y+h}{y_0+h}\right)\right]. \tag{4.12}$$

For $y_0 \le y < h$,

$$U_t(y) = -U_c + u_{\tau,t}\left[\frac{1}{\kappa}\ln\left(\frac{(h-y)u_{\tau,t}}{\nu}\right) + A - \frac{1}{3\kappa}\left(\frac{h-y}{h-y_0}\right)^3 + 2\frac{\Pi}{\kappa}\left(\frac{h-y}{h-y_0}\right)^2\left(3 - 2\frac{h-y}{h-y_0}\right)\right], \tag{4.13}$$

which automatically gives zero slope for both expressions at $y = y_0$. The velocity matching condition is again $U_b(y_0) = U_t(y_0)$. The slope matching condition is here replaced by matching the second derivatives at $y = y_0$, giving

$$\frac{u_{\tau,b}}{(h+y_0)^2} = \frac{u_{\tau,t}}{(h-y_0)^2}. \tag{4.14}$$

The third equation is (4.6), where $U(y)$ in the two ranges of integration is now given by (4.12) and (4.13), respectively. The integrations can again be performed analytically.

These three equations can again be cast in terms of independent variables (Re, θ) and dependent variables $(Re_{\tau,t}, Re_{\tau,b}, Y_0)$. These are summarized in Appendix B. With $\theta > \theta_c$, their numerical solutions are straightforward. For $\theta = 90°$, corresponding to pure Poiseuille flow, the model equations simplify and can be solved analytically, giving $Re_{\tau,b} = Re_{\tau,t}$, $Y_0 = 0$ and

$$Re_{\tau,t} = \frac{\kappa\, Re}{W(\exp(-13/12 + \Pi + A\kappa)\,\kappa\, Re)}. \tag{4.15}$$

Again, the limit $Re_{\tau,b} = 0$, $\theta = \theta_c$ can be explored. The resulting equations can be solved approximately by putting $\theta_c = \pi/4 - \epsilon$, $\epsilon \ll 1$. Linearizing in ϵ and solving the

https://doi.org/10.1017/jfm.2022.1023 Published online by Cambridge University Press

resulting equations gives

$$Re_{\tau,t} = \frac{\sqrt{2}\,\kappa\, Re}{W(2\sqrt{2}\exp(A\kappa - 13/12 + \Pi)\,\kappa\, Re)}, \tag{4.16}$$

$$\theta_c = \frac{\pi}{4} - \epsilon(Re), \tag{4.17}$$

where $\epsilon(Re)$ is a known but complicated function of Re that approaches 0 when $Re \to \infty$. Equation (4.16) does not agree with (4.9), but the mismatch is small and within the accuracy of the overall model. The reason is that velocity profiles with a wake component are used (and required) for Poiseuille flow $\theta > \theta_c$, but not for Couette-type flow $\theta < \theta_c$. The above model ignores the existence of a viscous sublayer expected near both walls when both $\ln[Re_{\tau,t}] \gg 1$ and $\ln[Re_{\tau,b}]| \gg 1$. This can be included, but makes negligible difference in numerical results when both $\ln(Re) \gg 1$, $\ln[Re_{\tau,b}] \gg 1$. This is, however, included near the bottom wall in the following model variation.

4.3. *PT-II: weakly Poiseuille-type flow, $Re_{\tau,b} \sim 0$*

It will be shown later that for $Re_{\tau,b} > 0$ small relative to its value for $\theta \to 90°$, model PT-I gives poor agreement with the present numerical simulation. This is because re-laminarization, when $\theta - \theta_c$ is positive but small, begins to be strongly affected by the pressure gradient, generating a near-wall maximum in the mean-flow velocity, as shown previously. To account for this, model PT-II replaces (4.13) with an approximate laminar profile obtained by putting $\overline{u'v'} = 0$ in the otherwise exact (3.6). Equation (4.12) is retained, as is the volume flow condition (4.6). The velocity matching condition at $y = y_0$ is unchanged, and the slope or gradient matching is now that $\mathrm{d}U(y)/\mathrm{d}y = 0$ at $y = y_0$ using the modified (3.6). This provides three closed equations for $Re_{\tau,b}$, $Re_{\tau,t}$ and Y_0, which are given in Appendix B. Numerical solutions are again straightforward. We note that as $\theta \to \theta_c$ from above, the gradient $d(Re_{\tau,b})/d\theta$ is singular as $(\theta - \theta_c)^{-1/2}$. This does not pose numerical problems. As with models CT and PT-I, the limit $Re \to \infty$ gives $\theta_c = \pi/4$.

4.4. *Infinite Re limit*

The limiting velocity in the bulk flow can be obtained by taking the $Re \to \infty$ limit of the velocity profiles given above. The analysis is similar for all cases, so we sketch one example to illustrate. With $Y = y/h$, (4.13) can be expressed as

$$\frac{U_t(y)}{U_0} = -\cos(\theta) + \frac{Re_{\tau,t}}{Re}\left(A - \frac{(Y-1)^2\,(Y - 1 + 6\,\Pi(1 + 2Y - 3Y_0))}{3\kappa\,(Y_0 - 1)^3} + \frac{\ln[Re_{\tau,t}(1-Y)]}{\kappa}\right). \tag{4.18}$$

In the large-Re limit, only the $\ln[Re_{\tau,t}]$ term inside the large parentheses survives, giving

$$\frac{U_t(y)}{U_0} = -\cos(\theta) - \frac{Re_{\tau,t}\ln(Re_{\tau,t})}{\kappa\, Re} + O\left(\frac{Re_{\tau_t}}{Re}\right), \tag{4.19}$$

independent of Y. This is true for all PCP flows considered presently. The large $\ln(Re)$ limit of the equation defining the solution for $Re_{\tau,t}$ is

$$Re_{\tau,t}\ln(Re_{\tau,t}) - Re\,\kappa(\sin\theta + \cos\theta) = 0. \tag{4.20}$$

https://doi.org/10.1017/jfm.2022.1023 Published online by Cambridge University Press

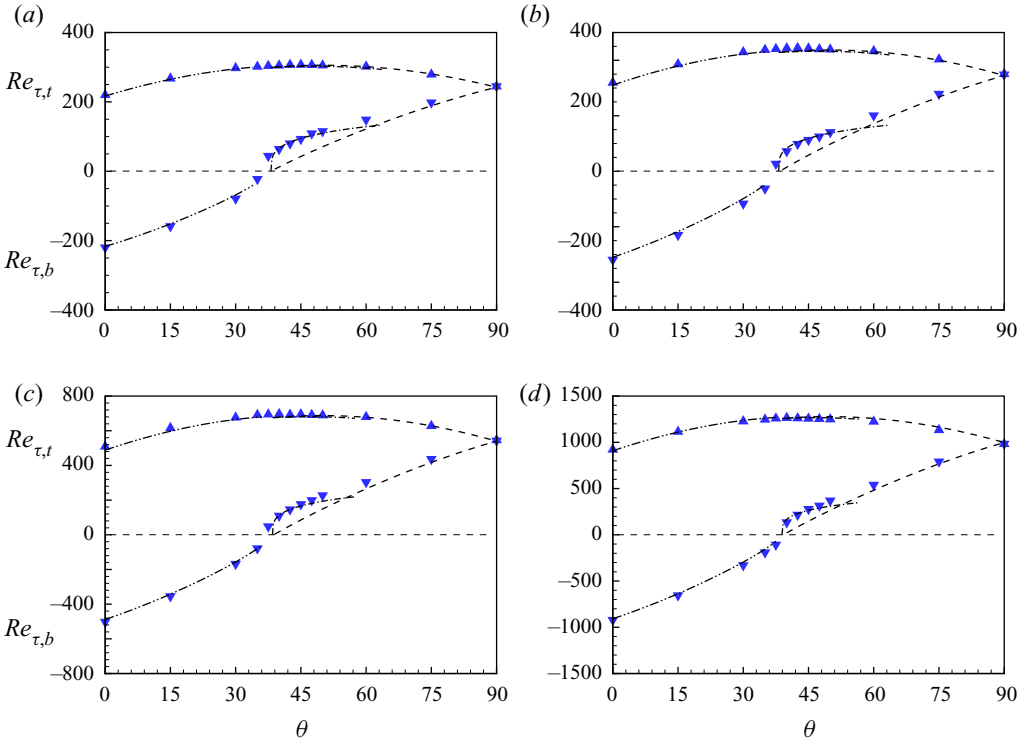

Figure 10. Friction Reynolds numbers for two walls, $Re_{\tau,t}$ (blue ▲) and $Re_{\tau,b}$ (blue ▼): (*a*) $Re = 4000$, (*b*) $Re = 6000$, (*c*) $Re = 10\,000$, (*d*) $Re = 20\,000$. Dash-dot-dotted lines indicate model CT; dashed lines indicate model PT-I; dash-dotted lines indicate model PT-II.

Using this result in (4.19) and taking the limit $Re \to \infty$ gives the plug-flow limiting velocity profile in the following alternative forms:

$$\frac{U_t(y)}{U_0} = \sin(\theta), \quad \frac{U_t(y)}{U_c} = \tan(\theta), \quad \frac{U_t(y)}{M/(2h)} = 1, \tag{4.21a–c}$$

which is consistent with $Re_M = Re\sin\theta$. This result can be obtained for both Couette- and Poiseuille-type flow for all $0^\circ \leq \theta < 90^\circ$. Detailed calculations are straightforward but are not developed presently. This gives the infinite-Re limiting velocity profile as plug flow for $-h < y < h$, except in vanishingly small viscous-type regions near both walls.

5. Properties of PCP flow

5.1. *Skin friction variation*

Figure 10 shows $Re_{\tau,b}$ and $Re_{\tau,t}$ versus θ for four Re values, consisting of DNS at $Re = 4000$, 6000 and WRLES data at $Re = 10\,000,\ 20\,000$. A general observation is that at the top wall, $Re_{\tau,t}$ is always positive; it varies slowly with increasing θ, but is not constant. For the bottom wall, $Re_{\tau,b}$ is equal and opposite to $Re_{\tau,t}$ at $\theta = 0^\circ$, but then increases monotonically as θ increases, passing through zero, and further increasing until $\theta = 90^\circ$, where $Re_{\tau,b} = Re_{\tau,t}$ for the turbulent Poiseuille-flow state. Model results are also shown. For $Re_{\tau,t}$, both the CT and PT-I turbulent models give accurate estimates over the whole range of θ. In calculating $Re_{\tau,t}$, differences between the PT-II and PT-I

https://doi.org/10.1017/jfm.2022.1023 Published online by Cambridge University Press

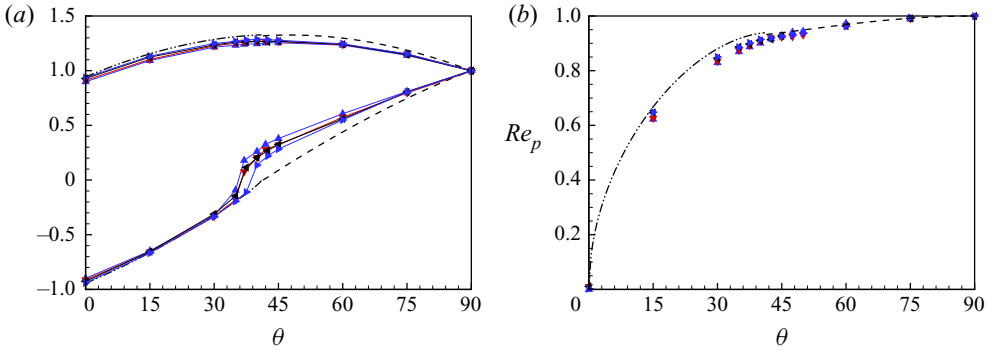

Figure 11. (*a*) Scaling of friction Reynolds numbers using values at $\theta = 90^\circ$: $Re_{\tau,t}/Re_{\tau,t}(90^\circ)$ for the top wall, and $Re_{\tau,b}/Re_{\tau,b}(90^\circ)$ for the bottom wall. (*b*) Reynolds number based on pressure, Re_p, where: ▲ indicates DNS of $Re = 4000$; ▼ indicates DNS of $Re = 6000$; ◀ indicates WRLES of $Re = 10\,000$; ▶ indicates WRLES of $Re = 20\,000$. Model prediction at $Re = 10^8$: dash-dot-dotted line indicates CT model; dashed line indicates PT-I model.

models are negligible. The maximum value of the relative error for $Re_{\tau,t}(\theta)$, between the model prediction and the simulation data, is around 2–3 %, and it slowly decreases with increasing Re. At the bottom wall, the CT model results show satisfactory agreement with simulation data for $Re_{\tau,b}$ up to $\theta = \theta_c$, where $Re_{\tau,b} = 0$.

For Poiseuille-type flow ($\theta > \theta_c$), the PT-I model agrees well with simulation for $\theta > 60^\circ$ but does not capture a hump in the $Re_{\tau,b}$ profile that appears for all four Re values for θ somewhat larger than θ_c. This is associated with a near-wall maximum in the mean velocity profile with laminar near-wall flow. For this range of θ where $\theta - \theta_c$ is greater than 0 but small, the PT-II model captures this sudden increase in $Re_{\tau,b}$ reasonably well, including its reduction in amplitude as Re increases. But PT-II is not appropriate for large θ owing to the assumed laminar profile near the bottom wall, so results using this model are shown over only a small θ range. A blended PT-I/PT-II model, uniformly valid for $Re_{\tau,b} > 0$, can be constructed but is not described presently. Both simulation and model indicate that $\theta_c(Re)$ increases with increasing Re, albeit very slowly. This will be revisited later when WMLES results for $\theta = \theta_c$ are discussed.

Figure 11(*a*) shows plots of both $Re_{\tau,t}/Re_{\tau,t}(\theta = 90^\circ)$ and $Re_{\tau,b}/Re_{\tau,b}(\theta = 90^\circ)$ versus θ, together with CT and PT-I model calculations for $Re = 10^8$. Reasonable collapse is obtained.

We have chosen Re_M, instead of the Reynolds number based on pressure gradient Re_p, as the independent parameter associated with mass flow generated by the finite pressure gradient. In figure 11(*b*), we show Re_p versus θ obtained from (2.5). Shown are numerical data from four Re values and one model prediction at $Re = 10^8$. The data are also scaled by their corresponding values at the Poiseuille case $\theta = 90^\circ$. Again, a reasonable collapse is obtained.

5.2. *Streamwise velocity change with* (Re, θ)

Figure 12 shows streamwise, mean velocity distributions $U(y/h)/U_0$ at $Re = 6000$ and 20 000 in $0^\circ \leq \theta \leq 90^\circ$ with increment 15°. Symbols show the simulation data. Profiles obtained from the three models are displayed as dashed lines. The Couette-type ($Re_{\tau,b} < 0$) model agrees quite well with the numerical results for $\theta = 0^\circ$, 15° and 30°, while the

https://doi.org/10.1017/jfm.2022.1023 Published online by Cambridge University Press

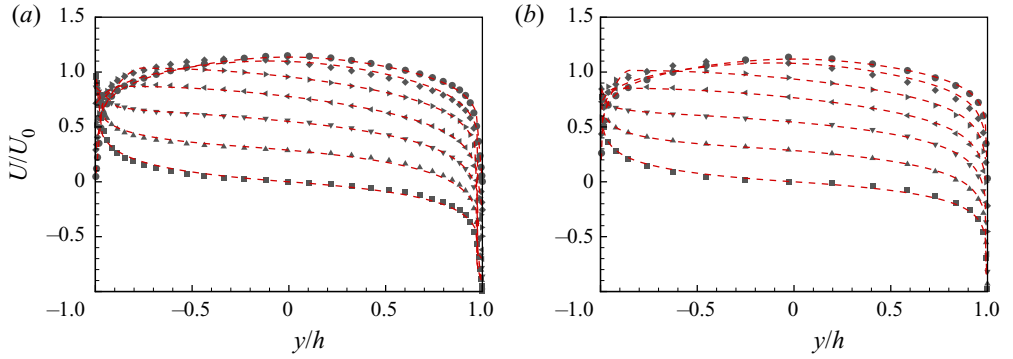

Figure 12. Comparison of streamwise velocity U/U_0 between model prediction and numerical results: (*a*) $Re = 6000$, (*b*) $Re = 20\,000$. Symbols for numerical results: ■, $\theta = 0°$; ▲, $\theta = 15°$; ▼, $\theta = 30°$; ◀, $\theta = 45°$; ▶, $\theta = 60°$; ◇, $\theta = 75°$; ●, $\theta = 90°$. Red dashed lines indicate model prediction profiles.

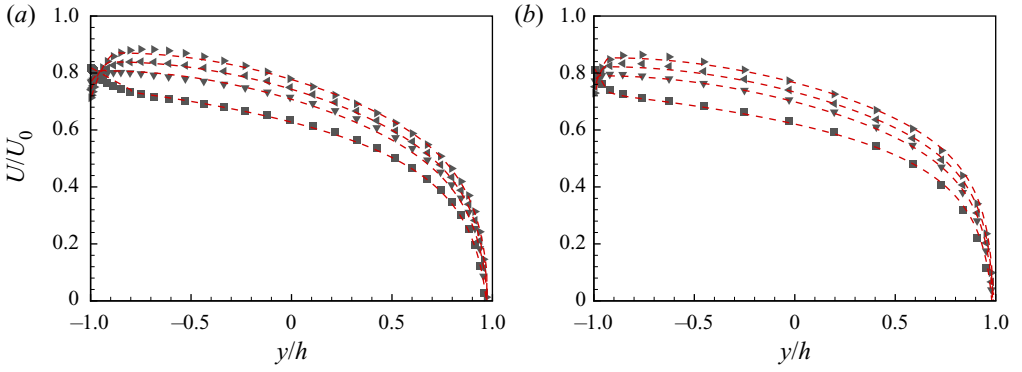

Figure 13. Comparison of streamwise velocity U/U_0 between model prediction and numerical results: (*a*) $Re = 6000$, (*b*) $Re = 20\,000$. Symbols for numerical results: ■, $\theta = 35°$; ▼, $\theta = 40°$; ◀, $\theta = 42.5°$; ▶, $\theta = 45°$. Red dashed lines indicate model prediction profiles.

strong Poiseuille-dominant model (PT-I, $Re_{\tau,b} \gg 0$) shows a good match with numerical data for $\theta = 90°$, and deviations appear near the bottom wall at $\theta = 60°, 75°$. To illustrate model performance near $\theta = \theta_c$, figure 13 shows $U(y/h)/U_0$ for $\theta = 35°$, $40°$, $42.5°$ and $45°$ for both $Re = 6000$ and $20\,000$. For flows with $Re_{\tau,b} > 0$, model PT-II provides satisfactory velocity profiles across the whole channel height.

5.3. *Turbulence intensities*

It is known that PC flow turbulence is generally not homogeneous in the spanwise direction owing to the existence of spanwise coherent rolls (Pirozzoli *et al.* 2014; Cheng *et al.* 2022). Two distinct spanwise averages can be defined. The first consists of streamwise, spanwise and time averaging, while the second excludes the spanwise average in order to recognize the spanwise non-homogeneity. For any instantaneous field $\Phi(x, y, z, t)$, with uniform time stepping, these are respectively

$$\bar{\Phi}(y) \equiv \frac{1}{N_t}\frac{1}{N_x}\frac{1}{N_z}\sum_{z,x,t}\Phi(x, y, z, t), \quad \hat{\Phi}(y, z) \equiv \frac{1}{N_t}\frac{1}{N_x}\sum_{x,t}\Phi(x, y, z, t), \qquad (5.1a,b)$$

https://doi.org/10.1017/jfm.2022.1023 Published online by Cambridge University Press

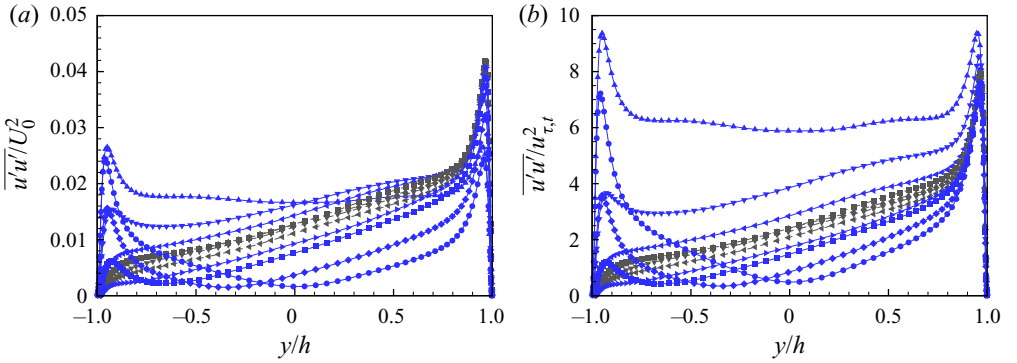

Figure 14. Distribution of streamwise turbulence intensities for $Re = 6000$: (*a*) $\overline{u'u'}/U_0^2$, (*b*) $\overline{u'u'}/u_{\tau,t}^2$. For symbol key, see figure 3.

with N_t the number of averaged time steps. The fluctuation field can also be defined in two ways:

$$\Phi'(x, y, z, t) \equiv \Phi(x, y, z, t) - \bar{\Phi}(y), \quad \Phi^{\bullet}(x, y, z, t) \equiv \Phi(x, y, z, t) - \hat{\Phi}(y, z). \quad (5.2a,b)$$

Further applying the $\bar{\Phi}$ operator produces two distinct Reynolds stress distributions: $\overline{u_i' u_j'}(y)$ and $\overline{u_i^{\bullet} u_j^{\bullet}}(y)$. The first describes fluctuations in a global sense, while the second shows only local fluctuations without recognition of variation that could be attributed to spanwise inhomogeneity.

The first distribution of streamwise turbulence intensity is shown in figure 14, for $Re = 6000$ across $0 \leq \theta \leq 90^\circ$ in outer scaling as $\overline{u'u'}/U_0^2$ and in top-wall inner scaling as $\overline{u'u'}/u_{\tau,t}^2$. The profile variations are symmetrical about $y = 0$ for $\theta = 0^\circ$ and 90°, but show substantial variation otherwise. A sharp maximum typical of wall-bounded turbulent flows is always present near the top wall. As θ increases, the magnitude of this peak in outer scaling first increases, reaches a local maximum at or very near the critical θ_c, and then decreases, behaviour similar to the variation of $Re_{\tau,t}(\theta)$. Using $u_{\tau,t}$ scaling, the peak magnitude decreases monotonically. Over the range $0^\circ \leq \theta \leq 45^\circ$, this can be ascribed to the attenuation of the large-scale rolls present for Couette-type flows, to be discussed subsequently. Over $45^\circ \leq \theta \leq 90^\circ$, it corresponds to the monotonic decrease of $Re_{\tau,t}$. Outboard of the peak, the general behaviour $\overline{u'u'}/u_{\tau,t}^2$ follows the peak as a monotonic decrease with increasing θ.

Near the bottom wall, the variation of the turbulence intensities with θ is qualitatively similar for both scalings, suggesting that they are not strongly influenced by the upper wall turbulence. The local maximum reduces rapidly as θ increases towards $\theta = \theta_c$, then vanishes as the flow laminarizes locally for θ near θ_c. The peak reappears as the near-wall flow re-transitions to a turbulent state when $\theta \to 90^\circ$. Scaling with $u_{\tau,b}$ is inappropriate across the whole range of θ owing to the laminar near-wall flow near $\theta = \theta_c$.

6. Transition from Couette-type to Poiseuille-type flow

It is known that large-scale spanwise rolls exist in PC flow (Pirozzoli *et al.* 2014; Lee & Moser 2018; Cheng *et al.* 2022) that enhance the turbulent mixing. These are not present for pure Poiseuille flow. Here, we explore flow changes as θ increases with Re fixed, and the flow transitions from a Couette-type to a Poiseuille-type state.

https://doi.org/10.1017/jfm.2022.1023 Published online by Cambridge University Press

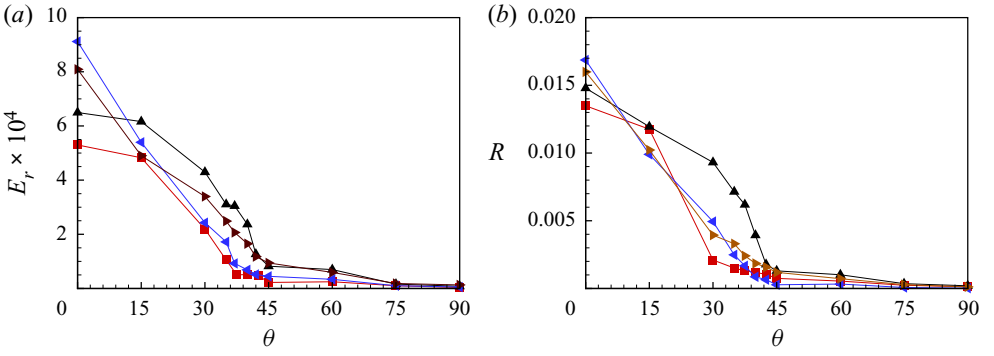

Figure 15. Cross-flow plane average diagnostics: (*a*) E_r, (*b*) R. Symbols: red ■, $Re = 4000$; black ▲, $Re = 6000$; blue ◀, $Re = 10\,000$; black ▶, $Re = 20\,000$.

6.1. *Average diagnostics*

For a velocity component $\hat{\Phi}(y, z)$ defined by (5.2*a*,*b*), we define its mean-flow energy as

$$E_\Phi = \frac{1}{4hL_z}\int_{-h}^{h}\int_{-L_z/2}^{L_z/2}\left(\frac{\hat{\Phi}(y,z)}{U_0}\right)^2 \mathrm{d}z\,\mathrm{d}y. \tag{6.1}$$

The choices $\hat{\Phi} = \hat{u}, \hat{v}, \hat{w}$ then give the mean-flow energies E_u, E_v, E_w associated respectively with the streamwise, wall-normal and spanwise directions. The sum $E_r = E_v + E_w$ is the energy in the mean flow in the (y, z) plane resulting from the presence (or otherwise) of large-scale spanwise rolls. Specifically, $E_r(Re, \theta)$ can be interpreted as the kinetic energy of the cross-flow, while $E_u(Re, \theta)$ is the streamwise energy.

In figure 15(*a*), we show $E_r(\theta)$. It is clear that the roll energy E_r generally declines to a small value at around the critical angle θ_c where $Re_{\tau,b} \sim 0$, and further decreases at around $\theta \approx 45°$. This suggests that the large-scale spanwise rolls generally exist only in the Couette-type flow domain. For $\theta > 45°$, the cross flow energy is finite but small. This can probably be attributed to the existence of residual break-up structures from spanwise rolls until $\theta \approx 75°$. The present trend of $E_r(\theta)$ is consistent with the time-averaged, cross-flow field obtained by Gandía-Barberá *et al.* (2018), where the roll structure gradually decays with increasing pressure gradient.

A further interesting diagnostic is the difference between the two turbulence intensities. An appropriate integral definition of the sum of the three difference components is

$$R = \frac{1}{2h}\int_{-h}^{h}\left(\frac{\overline{u_i'u_i'}(y) - \overline{u_i^\bullet u_i^\bullet}(y)}{U_0^2}\right)\mathrm{d}y. \tag{6.2}$$

In figure 15(*b*), we show the variation of R with θ for all four Re values. This shows a generally similar trend to the variation of $E_r(\theta)$ but with more statistical scatter.

6.2. *Instantaneous skin friction coefficient*

The instantaneous surface skin-friction field provides a useful indicator of the near-wall flow character. The two components of the skin-friction vector on the wall surface are C_{fx}

https://doi.org/10.1017/jfm.2022.1023 Published online by Cambridge University Press

and C_{fz}. For the top and bottom walls, we define

$$C_{fx,b} = \frac{\nu}{U_0^2}\left.\frac{\partial u}{\partial y}\right|_{-h}, \quad C_{fz,b} = \frac{\nu}{U_0^2}\left.\frac{\partial w}{\partial y}\right|_{-h}, \quad C_{fx,t} = \frac{\nu}{U_0^2}\left.\frac{\partial u}{\partial y}\right|_{h}, \quad C_{fz,t} = \frac{\nu}{U_0^2}\left.\frac{\partial w}{\partial y}\right|_{h}. \tag{6.3a–d}$$

Figure 16 shows colour-contour plots of $C_{fx,b}$ at a time instant for five flows with $Re = 6000$ and $\theta = 0^\circ, 37.5^\circ, 45^\circ, 60^\circ$ and 90°. For pure Couette flow with $\theta = 0^\circ$, footprints of the large-scale counter-rotating streamwise-oriented rolls with spanwise spacing of order $4h - 5h$ can be seen clearly. There are also small-scale structures that generally occupy the dividing region between large-scale rolls. Compared to Poiseuille flow at $\theta = 90^\circ$, those small-scale structures in Couette flow are more ordered, in both the streamwise and spanwise directions. At $\theta = 37.5^\circ$ where $u_{\tau,b} \sim 0$, the roll structures are clearly attenuated and are hardly observable. In fact, the skin-friction portrait appears to show small-scale structures oriented randomly in the plane. For $\theta = 45^\circ$, rolls are no longer visible. At $\theta = 60^\circ$, streamwise, streak-like structures have appeared, and at $\theta = 90^\circ$, these are fully developed with a spanwise spacing of order 100 viscous wall units, typical of classical wall-bounded turbulent flows. For clarity, we also show the corresponding colour-contour plots of $C_{fz,b}$ at the five θ values in figure 17. These show somewhat different structural features to the $C_{fx,b}$ portraits, but similar qualitative changes with increasing θ.

At $Re = 6000$, $\theta_c \approx 36.7^\circ$, where $Re_{\tau,b} \approx 0$. Here, in the frame of reference of the moving wall there is no mean-flow shear in both streamwise and spanwise directions. In figure 18, we show an image of the vector field lines of the instantaneous vector skin-friction coefficient $(C_{fx,b}, C_{fz,b})$ on the bottom wall, which are also limiting near-surface streamlines in the frame of reference where the bottom wall is stationary. For clarity, only a small rectangular domain of the bottom wall surface is shown. Bundles of separatrix-like structures together with spiral and saddle critical points (where $C_{fx,b} = C_{fz,b} = 0$) are visible, indicating local, small-scale separation–reattachment events. Orientations appear random. This near-bottom-wall flow is essentially random, unsteady three-dimensional laminar flow.

Figure 19 depicts the probability distribution functions (p.d.f.s) of both components of the skin-friction coefficients on the bottom wall across the range of θ for $Re = 6000$. In figure 19(*a*), as θ increases from 0° to 45°, the p.d.f. of $C_{fx,b}$ marches to the right towards zero mean at $\theta = \theta_c$ (black solid curve) with reducing variance and enhanced symmetry. The arrow indicates the trend with increasing θ. With θ increasing from 45° to 90°, the p.d.f. in figure 19(*b*) continues marching to the right with increasing variance and asymmetry. For $C_{fz,b}$ in figures 19(*c*,*d*), the p.d.f. curves remain symmetrical but show minimum variance at $\theta = \theta_c$. Skin-friction distributions at the upper wall in figure 20 show different behaviour. For θ increasing in $(0^\circ, 45^\circ)$, the p.d.f. of $C_{fx,t}$ marches to the right but retains left-leaning skewness. This trend is reversed as θ continues to increase in $(45^\circ, 90^\circ)$. The p.d.f. for $C_{fz,t}$ shows a variation with increasing θ that is reversed compared to that shown by $C_{fz,b}$. In the two limits – $\theta = 0^\circ$ for pure Couette flow, and $\theta = 90^\circ$ for pure Poiseuille flow – the p.d.f. curves of both skin-friction coefficients have very similar shapes except that p.d.f. curves of $C_{fx,b}$ are mirror-images for pure Couette flow.

https://doi.org/10.1017/jfm.2022.1023 Published online by Cambridge University Press

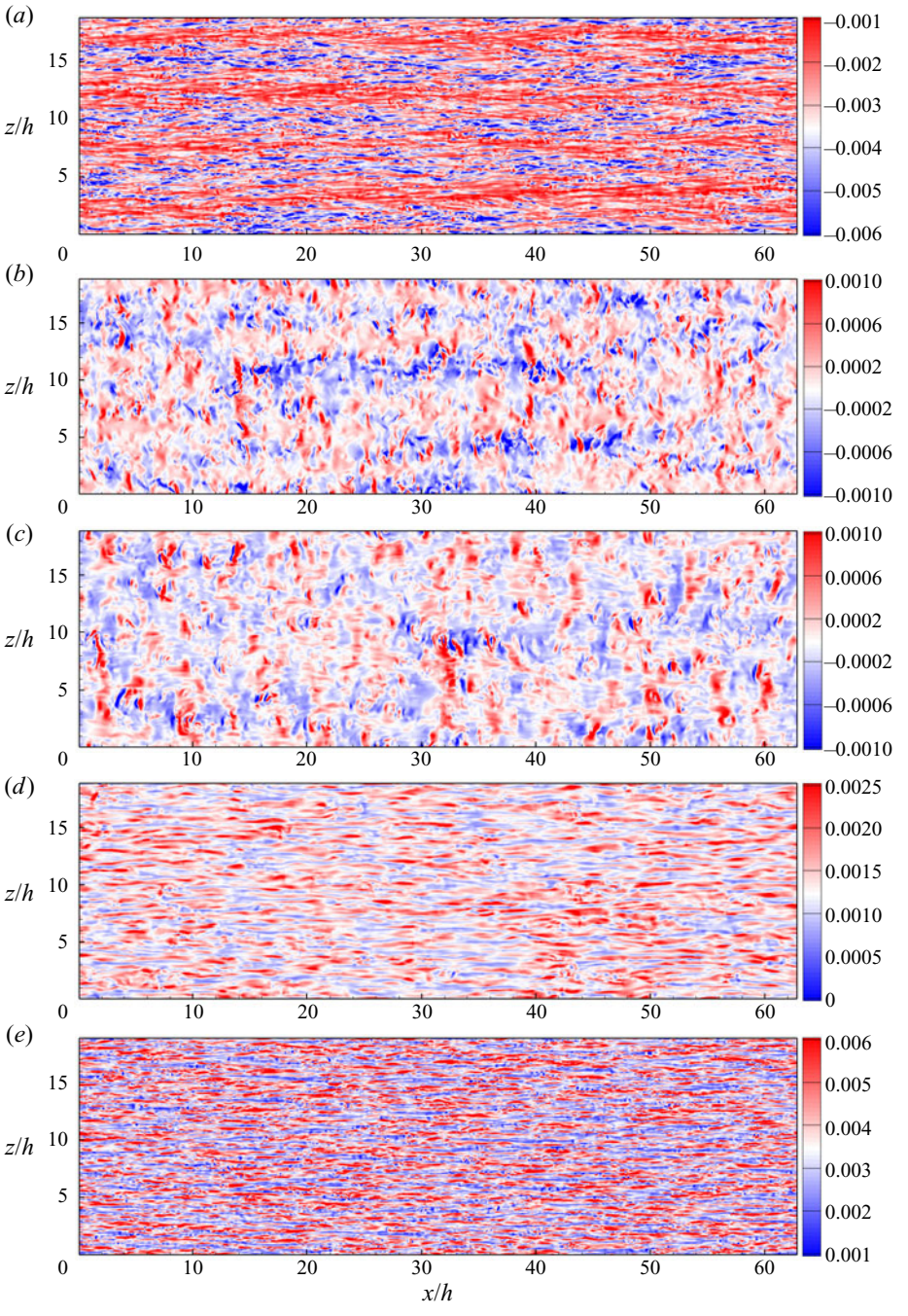

Figure 16. Colour contours of streamwise skin friction coefficient $C_{fx,b}$ on the bottom wall at $Re = 6000$: (*a*) $\theta = 0°$, (*b*) $\theta = 37.5°$, (*c*) $\theta = 45°$, (*d*) $\theta = 60°$, (*e*) $\theta = 90°$.

6.3. *Flow visualization*

Visualizations such as iso-surface structures can provide a three-dimensional perspective. In figure 21, we compare iso-surface plots of the wall-normal velocity v at $v = -0.02U_0$

https://doi.org/10.1017/jfm.2022.1023 Published online by Cambridge University Press

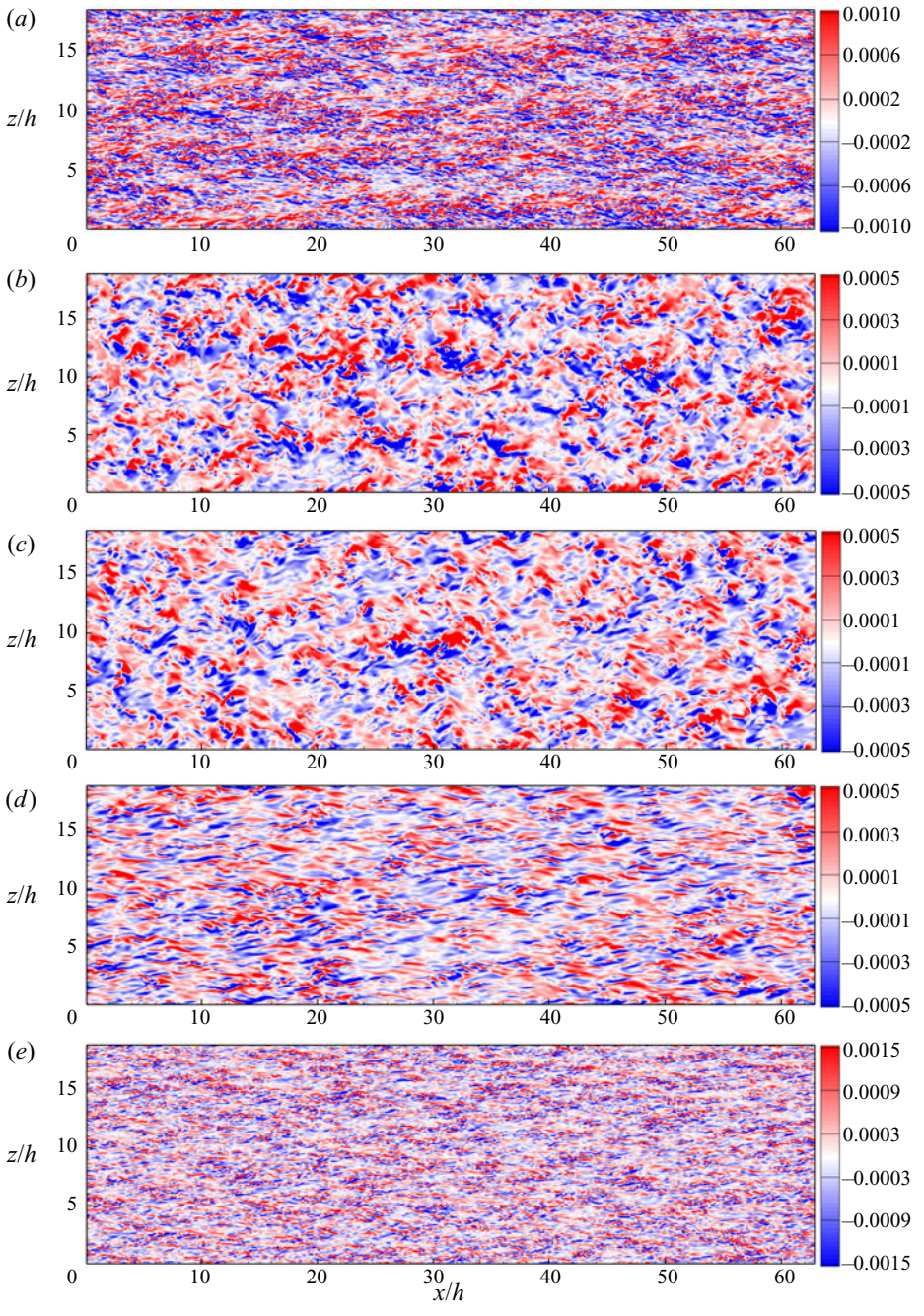

Figure 17. Colour contours of spanwise skin friction coefficient $C_{fz,b}$ on the bottom wall for $Re = 6000$: (*a*) $\theta = 0^\circ$, (*b*) $\theta = 37.5^\circ$, (*c*) $\theta = 45^\circ$, (*d*) $\theta = 60^\circ$, (*e*) $\theta = 90^\circ$.

obtained from time-window-averaged flow fields at $Re = 4000$, with visualization over the whole computational domain. The average time frame is approximately one turnout time, approximately $U_c T/L_x \cos\theta = 1$. Five cases include $\theta = 0^\circ$, 15°, 45°, 60° and 75°.

https://doi.org/10.1017/jfm.2022.1023 Published online by Cambridge University Press

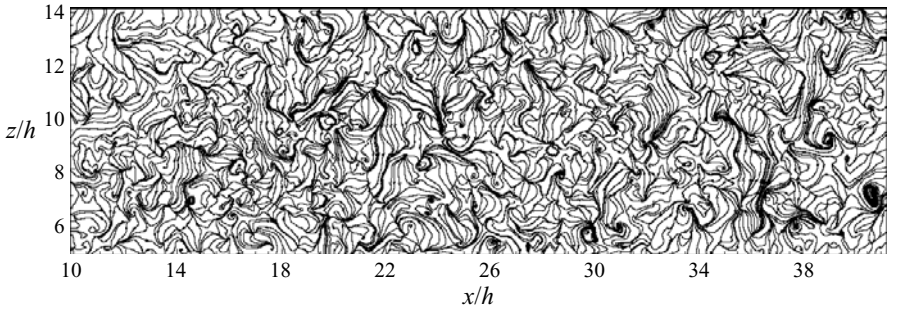

Figure 18. Instantaneous skin friction lines on the bottom wall for $\theta = 37.5^\circ$ at $Re = 6000$.

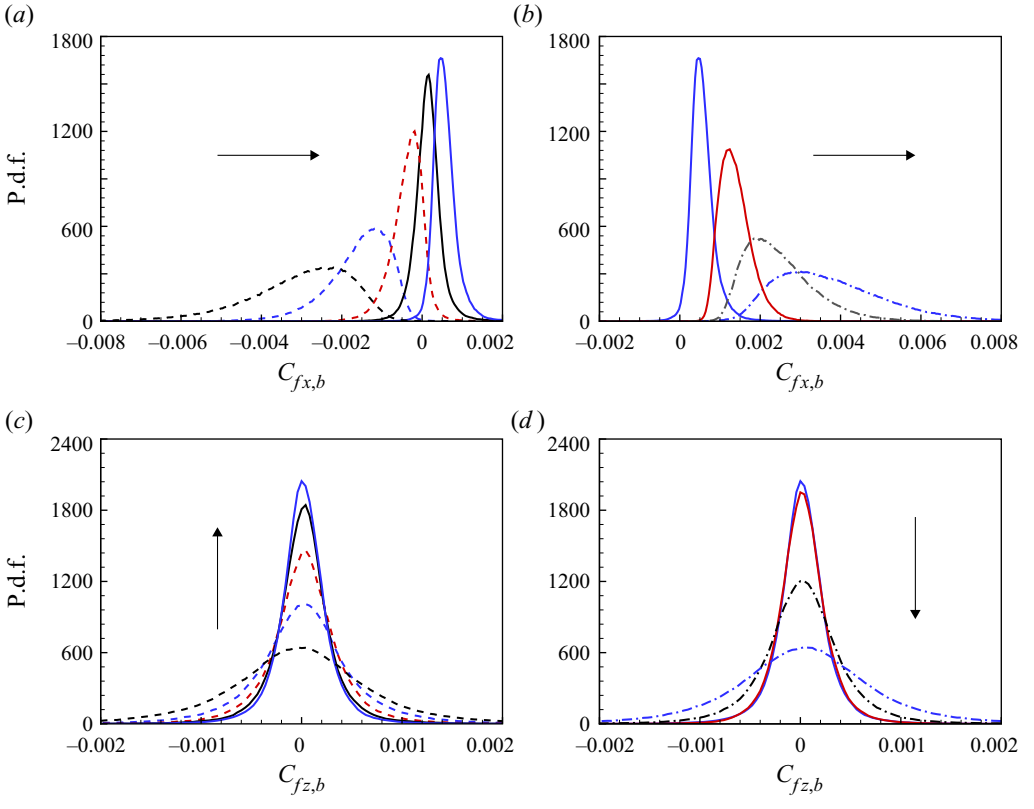

Figure 19. P.d.f.s of skin-friction coefficients at the bottom wall: (*a*) $C_{fx,b}$ from $\theta = 0^\circ$ to 45°; (*b*) $C_{fx,b}$ from $\theta = 45^\circ$ to 90°; (*c*) $C_{fz,b}$ from $\theta = 0^\circ$ to 45°; (*d*) $C_{fz,b}$ from $\theta = 45^\circ$ to 90°. Dashed lines: black, $\theta = 0^\circ$; blue, $\theta = 15^\circ$; red, $\theta = 30^\circ$. Solid lines: black, $\theta = 37.5^\circ$; blue, $\theta = 45^\circ$; red, $\theta = 60^\circ$. Dash-dotted lines: black, $\theta = 75^\circ$; blue, $\theta = 90^\circ$.

For Couette-type flows of $\theta = 0^\circ$ and $\theta = 15^\circ$, the signatures of streamwise structures are clearly visible, while for $\theta = 45^\circ$, these structures have been greatly attenuated. Cases $\theta = 60^\circ$ and $\theta = 75^\circ$ show almost no identifiable structure.

https://doi.org/10.1017/jfm.2022.1023 Published online by Cambridge University Press

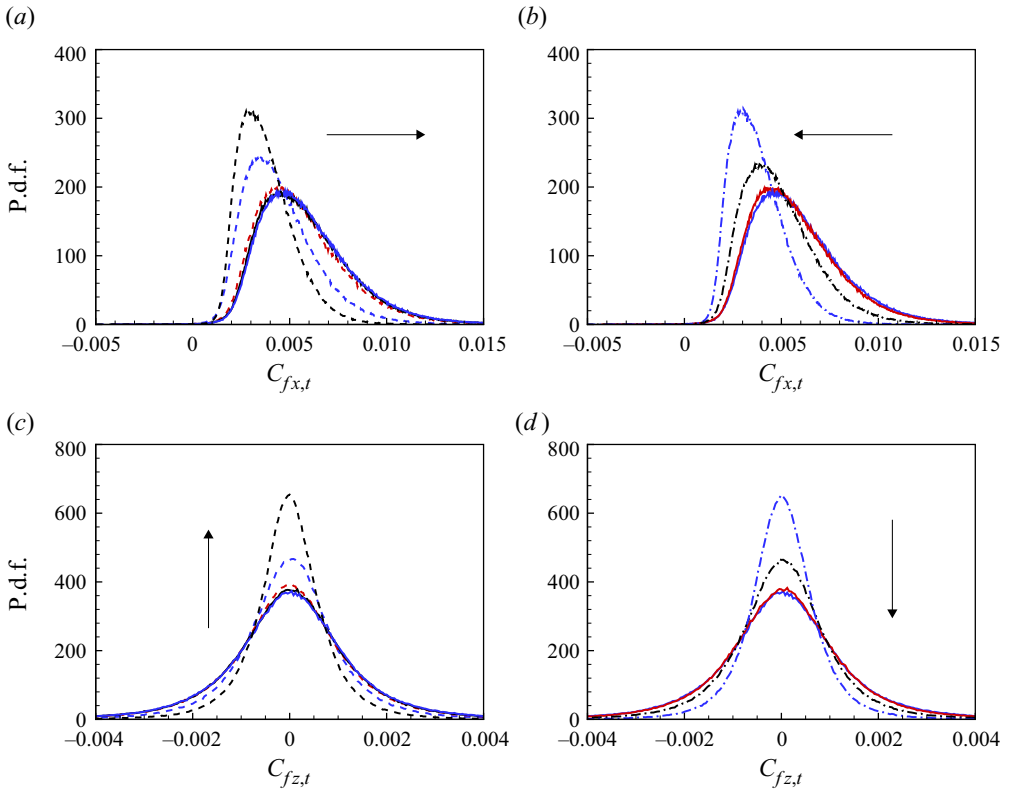

Figure 20. P.d.f.s of skin-friction coefficients at the top wall: (*a*) $C_{fx,t}$ from $\theta = 0^\circ$ to 45°; (*b*) $C_{fx,t}$ from $\theta = 45^\circ$ to 90°; (*c*) $C_{fz,t}$ from $\theta = 0^\circ$ to 45°; (*d*) $C_{fz,t}$ from $\theta = 45^\circ$ to 90°. For line types, refer to figure 19.

7. Flow with zero skin friction on the bottom wall

Here, we discuss flow properties along the trajectory in the (Re, θ) plane where $Re_{\tau,b} = 0$. These are referred to as zero skin friction (ZSF) flows. This is done to limit computational expenditure for a two-parameter flow yet provide simulation data that characterize an interesting example of a wall-bounded turbulent flow over a range of Re that exceeds bounds attainable with DNS and with WRLES. Simulations were performed at Re values shown in table 1, where the methodology is also indicated.

In simulation, the ZSF condition is enforced by fixing Re and employing a control algorithm to vary the mean pressure gradient to control θ dynamically during simulation until $Re_{\tau_b}(\theta) \approx 0$ is found. The control algorithm consists of a penalty method implementation which dynamically adjusts the mean pressure gradient at every time step to optimize the averaged velocity gradient on the bottom wall. As discussed earlier, experiences with the PT-II model and numerical simulation suggest that at $\theta = \theta_c$, $\mathrm{d}(Re_{\tau,b})/\mathrm{d}\theta$ on the Poiseuille side is singular as $(\theta - \theta_c)^{-1/2}$ when $Re_{\tau,b} \to 0$. This, plus the fact that the time-planar average used for wall shear stresses itself exhibits inevitable fluctuations, has the effect that convergence to $Re_{\tau,b} = 0$ to machine precision has not been achieved. In practice, an accuracy $|Re_{\tau_b}|/Re_{\tau_t} \sim O(10^{-3})$ is obtained. For WMLES, the wall model is turned on only at the upper wall.

https://doi.org/10.1017/jfm.2022.1023 Published online by Cambridge University Press

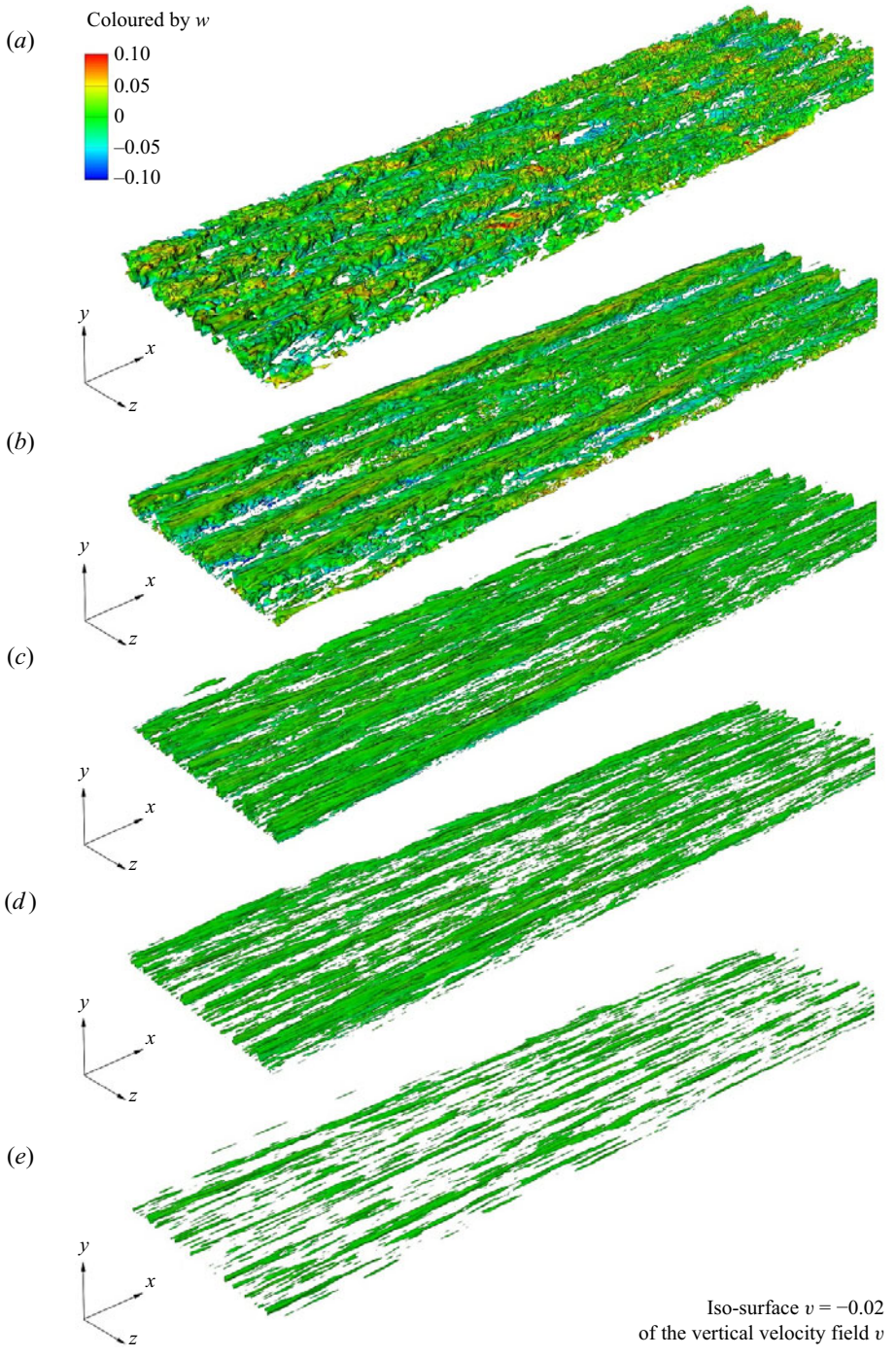

Figure 21. Visualization of time-averaged vertical velocity fields v with colouring by spanwise velocity w at $Re = 4000$: (*a*) $\theta = 0°$, (*b*) $\theta = 15°$, (*c*) $\theta = 45°$, (*d*) $\theta = 60°$, (*e*) $\theta = 75°$.

https://doi.org/10.1017/jfm.2022.1023 Published online by Cambridge University Press

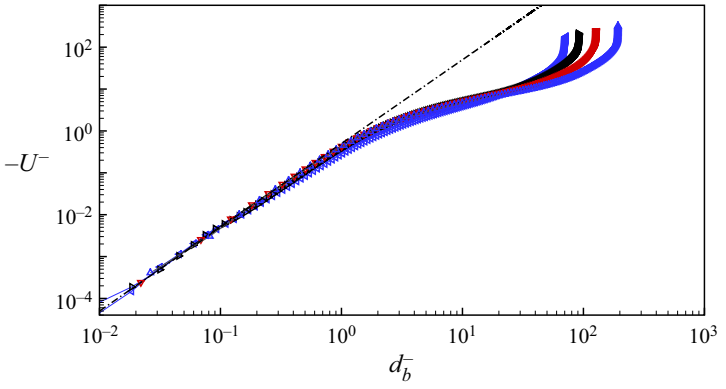

Figure 22. Scaled velocity profile near the bottom wall: U^- versus d_b^-. Symbols: blue ◁, 4000; black ▷, 6000; red ▽, 10 000; blue △, 20 000. Dash-dotted line indicates $U^- = -(d_b^-)^2/2$.

7.1. *Bottom wall (U^-, d_b^-) scaling*

For ZSF flows, $u_{\tau,b} = 0$, indicating the absence of a local wall-velocity scale. Following Stratford (1959), Coleman *et al.* (2017) investigated the near-bottom-wall flow at Re_c up to 1.2×10^4 in terms of the alternative, pressure-gradient-based scaling

$$U^- \equiv \frac{u(d_b) - U_c}{u_p} = f(d_b^-), \quad d_b^- \equiv \frac{d_b\, u_p}{\nu}, \quad u_p \equiv \left(\nu \left|\frac{\mathrm{d}}{\mathrm{d}x}\left(\frac{p}{\rho}\right)\right|\right)^{1/3}. \tag{7.1a–c}$$

From the integrated skin-friction–pressure-gradient balance for the whole channel, we find that

$$u_p = \left(\frac{\nu\, u_{\tau,t}^2}{2h}\right)^{1/3}, \quad \frac{u_p}{u_{\tau,t}} = \frac{1}{\left(2\, Re_{\tau,t}\right)^{1/3}}. \tag{7.2a,b}$$

Using (3.6) with $u_{\tau,b} = 0$, neglecting the Reynolds stress term and normalizing using the (U^-, d_b^-) scaling, gives

$$U^- = -\tfrac{1}{2}\left(d_b^-\right)^2. \tag{7.3}$$

Figure 22 shows the present DNS/WRLES mean velocity profiles near the bottom wall in (U^-, d_b^-) scaling. The profiles collapse well and agree with (7.3) over almost two decades of d_b^-. Our WMLES do not provide sufficient near-wall resolution to test this scaling.

7.2. *Streamwise velocity profiles for ZSF flows*

Streamwise velocity profiles are shown in figure 23(*a*) in top-wall inner scaling units. A logarithmic profile with $U^+ = 1/0.4 \ln y^+ + 5.0$ is also displayed. For our smallest $Re = 100$ and 300, the channel flow is essentially laminar, as shown in the kicked-up profiles at small d_t^+. At larger Re up to $Re = 10^{10}$ with $Re_{\tau_t} \approx 2.72 \times 10^8$, the velocity profiles match the log profile across almost the whole channel height of $2h$. Figure 23(*b*) shows velocity profiles in outer scaling as $U(y/h)/(U_c$ versus y/h, where it is noted that $\theta_c = \theta_c(Re)$ varies with Re. Also shown are mean-flow model predictions using PT-II. Model predictions are also shown for $Re = 10^{20}, 10^{50}, 10^{100}$. These show an asymptotic

https://doi.org/10.1017/jfm.2022.1023 Published online by Cambridge University Press

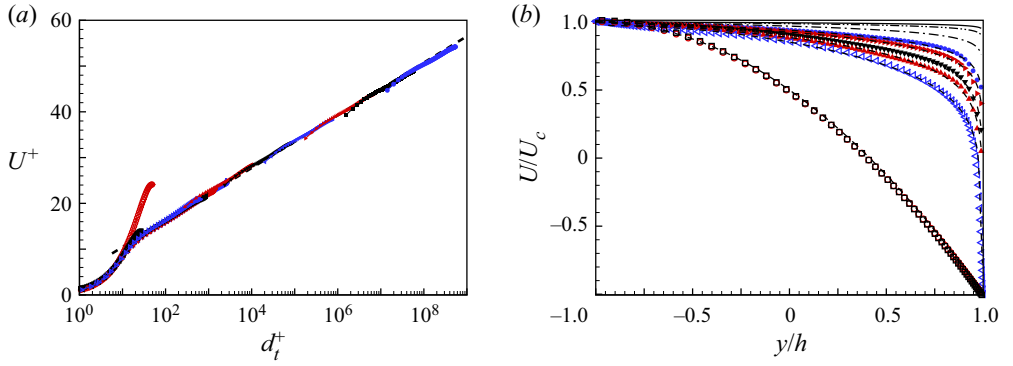

Figure 23. Streamwise velocity profiles of ZSF flows: (*a*) U^+, where the dashed line is the logarithmic line $U^+ = 1/0.4 \ln y^+ + 5.0$; (*b*) model prediction of velocity profiles up to $Re = 10^{100}$, where the dashed line is the model prediction profile for corresponding *Re*. Symbols for *Re* values: black □, 100; red ○, 300; blue ◁, 4000; black ▷, 6000; red ▽, 10 000; blue △, 20 000; red ▲, 10^5; black ▼, 10^6; blue ◀, 10^7; red ▶, 10^8; black ■, 10^9; blue ●, 10^{10}. Cases with only model prediction: dash-dotted line, 10^{20}; dash-dot-dotted line, 10^{50}; solid line, 10^{100}.

approach to $U/U_0 = \sin\theta$ when $Re \to \infty$ as stated by (4.21*a–c*). Since, as discussed subsequently, $\theta_c \to 45^\circ$ when $Re \to \infty$, the limit streamwise velocity for ZSF flows is $U(y/h) \to U_c$ except in a thin viscous layer at the top wall. The thickness of this layer as a function of *Re* can be estimated, an exercise left to the reader. Approach to the limit is extremely slow. Further, for ZSF flows, (2.5) gives $Re_p = Re_{\tau,t}/\sqrt{2}$ so that $Re_p/Re \to 0$ as $Re \to \infty$.

Figure 23(*b*) also suggests a simple interpretation of the result $\theta_c \to 45^\circ$ when $Re \to \infty$ for flows with $Re_{\tau,b} = 0$. The limiting plug-flow velocity $U(y) = U_c$ is the only velocity that satisfies both the Dirichlet boundary and also $\mathrm{d}U/\mathrm{d}y = 0$ on the bottom plate. Then if $U(y) = U_c$, the volume flow rate is $M = 2hU_c$. So then $Re_c = U_c h/\nu$ and $Re_M = M/(2\nu) = U_c h/\nu$. So in the large-*Re* limit, $Re_c = Re_M$ for ZSF flows, which means $\theta = 45^\circ$.

7.3. *Skin friction and mean-flow square velocity*

The variation of the critical angle $\theta_c(Re)$ is shown in figure 24(*a*), where the square symbols are DNS results, the two triangles give WMLES results, and the circles show the six WMLES results. For strictly laminar PCP flow, $\theta_c \approx 18.4^\circ$ (see Appendix A) independent of *Re*. Simulations at $Re = 100$ and 300 show consistency with this value. At $Re = 1000$, $\theta_c \approx 33^\circ$, while at $Re = 4000$, the bulk flow has transitioned to turbulence with $\theta_c \approx 36^\circ$. As *Re* increases further, the simulations show a monotonic increase in θ_c. Predictions for the three models CT and PT-I are shown. All models indicate $\theta_c \to 45^\circ$ as $Re \to \infty$, but it is apparent that the limit approach is sub-logarithmic as indicated by (4.10). The top-wall skin-friction variation for ZSF flows is displayed in figure 24(*b*), where again both laminar and the present model profiles are shown for comparison. The two models agree to plotting accuracy .

Using the model skin friction law and velocity profile, an estimate of the streamwise mean-flow square velocity can be made. For strict PC flow at $\theta = 0^\circ$, the $Re \to \infty$ asymptotic velocity in the bulk flow is 0 except in thin viscous-dominated layers near the two moving walls. In the frame of reference of the moving bottom wall, the asymptotic

https://doi.org/10.1017/jfm.2022.1023 Published online by Cambridge University Press

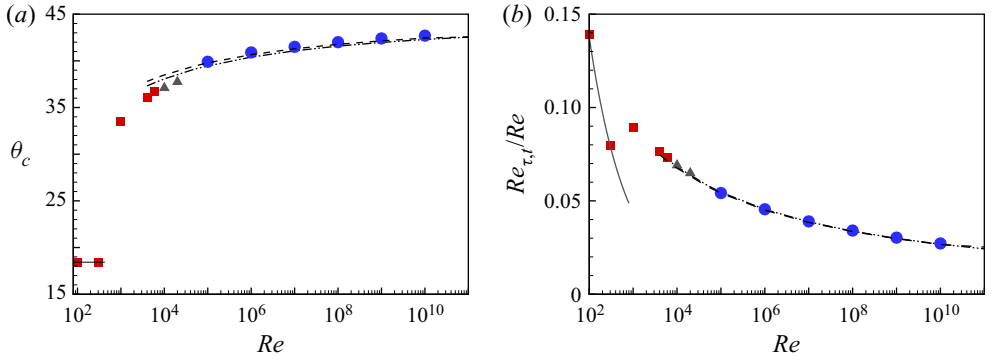

Figure 24. Skin-friction property of ZSF flows: (*a*) critical angle θ_c; (*b*) skin-friction $Re_{\tau,t}/Re$. Dashotted line indicates laminar exact solution. Turbulent modelling prediction: dash-dot-dotted line, CT model; dashed line, PT-I model. Symbols: red ■, DNS; black ▲, WRLES; blue •, WMLES.

mean velocity profile for ZSF flow is $U(y) \to 0$ except in the thin layer near the top wall. Using the model velocity profile (4.18) corrected for the bottom-wall reference frame, and the asymptotic expression (4.9), a scaled mean-flow streamwise square velocity for ZSF flow in the limit $Re \to \infty$ can be obtained as

$$E = \frac{1}{2h}\int_{-h}^{h}\left(\frac{U(y)}{u_{\tau,t}}\right)^2 \mathrm{d}y \to \frac{2}{\kappa^2}. \tag{7.4}$$

This result states that in the frame of reference of the asymptotic, plug-flow velocity, the streamwise mean-flow square velocity scales on $u_{\tau,t}^2$. This agrees with similar analysis for pure Couette flow.

7.4. *Turbulence intensities*

For ZSF flows, we expect turbulence intensity profiles to be typical of boundary layer flows except perhaps near the bottom wall, where the flow is laminar over a small region of extent that reduces with respect to the channel width as Re increases. These are shown in figure 25(*a*) for the four DNS/WRLES values of Re. They show an expected inner peak, with its magnitude growing slowly with increasing Re, existing at approximately constant $d_t^+ \approx 15$ together with an incipient plateau forming at $Re = 20\,000$. The DNS/WRLES do not reach sufficiently large Re to test the appearance of an outer peak. Intensities for WMLES are displayed together with DNS/WRLES profiles in outer coordinate scaling in figure 25(*b*). All results show good collapse away from the top wall. Near the bottom wall, all profiles display a steep decrease from approximately $\overline{u'u'}/u_{\tau,t}^2 \sim 1$ to 0 over the near-wall laminar flow.

8. Conclusion

We have investigated the properties of turbulent PCP flow between two moving plates separated by distance $2h$, where the plate velocity difference and the applied pressure gradient are aligned. Both numerical simulation and mean-flow modelling are used in a two-dimensional parameter space with plate velocity and volume-flow-rate Reynolds numbers (Re_c, Re_M), respectively, or equivalently, (Re, θ) with $Re_c = Re\cos\theta$,

https://doi.org/10.1017/jfm.2022.1023 Published online by Cambridge University Press

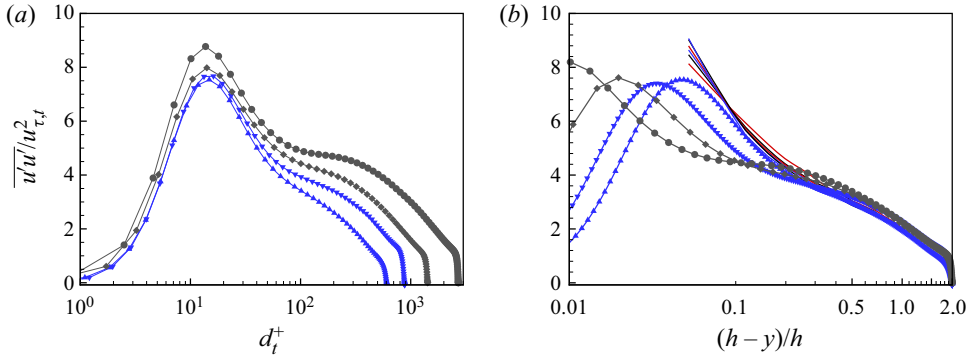

Figure 25. Streamwise turbulence intensity profiles for ZSF flows: (*a*) $\overline{u'u'}/U_{\tau,t}^2$ versus d_t^+; (*b*) $\overline{u'u'}/U_{\tau,t}^2$ versus $(h-y)/h$. Symbols: blue ▲, $Re = 4000$; blue ▼, $Re = 6000$; black ♦, $Re = 10\,000$; black •, $Re = 20\,000$. Solid lines: red, $Re = 10^5$; black, $Re = 10^6$; blue, $Re = 10^7$. Dashed lines: red, $Re = 10^8$; black, $Re = 10^9$; blue, $Re = 10^{10}$.

$Re_M = Re \sin\theta$. The simulations use DNS, WRLES and WMLES. The stretched-spiral vortex SGS model provides the subgrid scale turbulence effect in WRLES and WMLES.

The present numerical modelling of parallel PCP flow covers a fairly wide range of Reynolds numbers. This includes DNS at $Re = 4000$ and 6000, WRLES at $Re = 10\,000$ and 20 000, and WMLES cases for flows with zero skin friction on the bottom wall with Re up to 10^{10}. The goal has been to provide a comprehensive picture of PCP flows on the (Re, θ) parameter plane together with a focused study of PCP flow with one zero-skin-friction wall, over a larger Reynolds number range.

The general behaviour of PCP flow is characterized by a competition between the dominance of the applied pressure gradient and flow shear provided by the forced plate velocity difference. At fixed Re in the bulk-flow turbulence regime, as θ increases from 0° to 90°, the flow undergoes a change from a Couette- to a Poiseuille-type state. On the lower wall, the shear stress passes through zero at an angle θ_c that depends on Re. Velocity profiles away from this wall and towards the top wall are always turbulent, with a consistently elongated logarithmic region. As θ passes through θ_c, the flow near the bottom wall de-transitions to a laminar state where the effects of the pressure gradient and shear provided by the plate velocity difference are in approximate balance. Over a small range of θ, the production of energy associated with unsteady, fluctuation flow becomes negative, at least for $Re = 6000$. With further increase in θ, the near-bottom-wall flow then re-transitions to turbulence in the Poiseuille-type region of the (Re, θ) plane. This change of state is accompanied by the rapid attenuation and quashing of streamwise-oriented and spanwise-spaced flow rolls present in Couette-type flow. This observation is supported by energy-based diagnostics and flow visualization.

Three relatively simple three-equation mean-flow models are developed based on standard log-wake laws, and for one model, an approximate near-wall laminar velocity profile. It is argued that the models are physically appropriate in various regions on the (Re, θ) plane with changeover near the curve where the skin friction on the lower wall is zero. The models are shown to give good estimates of mean-flow properties as obtained from the numerical simulations. These include mean-flow velocity profiles, skin-friction Reynolds numbers on both walls, and the functional variation of $\theta_c(Re)$. Model extrapolation to the infinite Re limit indicates plug-like mean flow for all cases.

https://doi.org/10.1017/jfm.2022.1023 Published online by Cambridge University Press

DNS, WRLES and WMLES are used to study the subset of PCP flows where the skin friction on the lower wall is zero, up to $Re = 10^{10}$. Very near the bottom wall, the mean velocity profiles show collapse on a velocity scale that depends on both the viscosity and the magnitude of the applied pressure gradient, and that agrees with a quadratic variation, based on locally laminar flow, with the dimensionless wall-normal distance. These zero-friction flows show an overall log-like mean velocity region based on the upper-wall friction velocity that extends over much of the flow domain. Their mean-flow properties are well predicted by the models developed. The ratio of the upper-wall friction Reynolds number to Re follows an inverse ProductLog dependence on Re and $\theta_c \to 45^\circ$ when $Re \to \infty$.

Funding. This work was supported by the National Natural Science Foundation of China (nos 12172352, 91952205 and 11621202). The Cray XC40, Shaheen, at KAUST was utilized for the reported DNS and WRLES.

Declaration of interests. The authors report no conflict of interest.

Author ORCIDs.
W. Cheng https://orcid.org/0000-0003-3960-4162;
R. Samtaney https://orcid.org/0000-0002-4702-6473;
X. Luo https://orcid.org/0000-0002-4303-8290.

Appendix A. Laminar PCP flow

The laminar-flow solution is the superposition of PC and PP flow. This can be written as

$$\frac{U(y)}{U_0} = -Y\cos\theta + \frac{3}{2}(1-Y^2)\sin\theta, \tag{A1}$$

where $Y = y/h$ and $U_0 = U_c/\cos\theta$. Laminar-flow friction Reynolds numbers can then be obtained as

$$Re_{\tau,t} = (Re(\cos\theta + 3\sin\theta))^{1/2}, \tag{A2}$$

$$Re_{\tau,b} = (Re(\cos\theta - 3\sin\theta))^{1/2}, \quad \theta < \arctan(1/3), \tag{A3}$$

$$Re_{\tau,b} = (Re(-\cos\theta + 3\sin\theta))^{1/2}, \quad \theta > \arctan(1/3), \tag{A4}$$

and for laminar flow, $\theta_c = \arctan(1/3) = 18.435^\circ$ independent of Re. Alternative expressions are

$$Re_{\tau,t} = (3Re_M + Re_c)^{1/2}, \quad Re_{\tau,b} = \frac{3Re_M - Re_c}{|3Re_M - Re_c|^{1/2}}. \tag{A5a,b}$$

When $Re_{\tau,b} = 0$, (A6) can be written as

$$\frac{U(y)}{U_0} = \frac{3}{\sqrt{10}}\left(-Y + \frac{1}{2}(1-Y^2)\right). \tag{A6}$$

Also, Re_p of (2.5) is $Re_p^2 = 3Re_M$, while $Re_{\tau,t} = (2Re_c)^{1/2} = (6Re_M)^{1/2}$.

https://doi.org/10.1017/jfm.2022.1023 Published online by Cambridge University Press

Appendix B. Equations for PT-I and PT-II models

B.1. *PT-I model*

The velocity matching equation is

$$6\kappa\, Re\cos\theta + (6\Pi + 3A\kappa - 1)\left(Re_{\tau,b} - Re_{\tau,t}\right) + 3Re_{\tau,b}\ln[Re_{\tau,b}(1+Y_0)] - 3Re_{\tau,t}\ln[Re_{\tau,t}(1-Y_0)] = 0, \tag{B1}$$

while the matching of the second velocity gradients at $y = y_0$ gives

$$Y_0 = \frac{Re_{\tau,b}^{1/2} - Re_{\tau,t}^{1/2}}{Re_{\tau,b}^{1/2} + Re_{\tau,t}^{1/2}}. \tag{B2}$$

The equation obtained from the definition of Re_M is

$$24\kappa\, Re(\sin\theta - Y_0\cos\theta) - Re_{\tau,b}(1+Y_0)\left(-13 + 12A\kappa + 12\Pi + 12\ln[Re_{\tau,b}(1+Y_0)]\right) + Re_{\tau,t}(-1+Y_0)\left(-13 + 12A\kappa + 12\Pi + 12\ln[Re_{\tau,t}(1-Y_0)]\right), \tag{B3}$$

where Y_0 is given by (B2).

B.2. *PT-II model*

The velocity matching equation is

$$4(6\Pi - 1)\,Re_{\tau,t} + 3\kappa\big(-8\,Re\cos\theta + Re_{\tau,b}^2\,(Y_0-3)(Y_0+1) + Re_{\tau,t}\,(4A + Re_{\tau,t}(1+Y_0)^2)\big) + 12\,Re_{\tau,t}\ln[Re_{\tau,t}\,(1-Y_0)], \tag{B4}$$

while the matching of the second velocity gradients at $y = y_0$ gives

$$Y_0 = \frac{Re_{\tau,b}^2 - Re_{\tau,t}^2}{Re_{\tau,b}^2 + Re_{\tau,t}^2}. \tag{B5}$$

The equation obtained from the definition of Re_M is

$$(12\Pi - 13)(Y_0-1)\,Re_{\tau,t} + \kappa\,(24\,Re\,(\sin\theta - Y_0\cos\theta) + Re_{\tau,b}^2\,(Y_0-5)(1+Y_0)^2 + Re_{\tau,t}\left(12A(Y_0-1) + Re_{\tau,t}\,(Y_0+1)^3\right)) + 12Re_{\tau,t}(Y_0-1)\ln[Re_{\tau,t}\,(1-Y_0)], \tag{B6}$$

where Y_0 is given by (B5).

References

Andreolli, A., Quadrio, M. & Gatti, D. 2021 Global energy budgets in turbulent Couette and Poiseuille flows. *J. Fluid Mech.* **924**, A25.

Avsarkisov, V., Hoyas, S., Oberlack, M. & García-Galache, J.P. 2014 Turbulent plane Couette flow at moderately high Reynolds number. *J. Fluid Mech.* **751**, R1.

Bottin, S., Dauchot, O., Daviaud, F. & Manneville, P. 1998 Experimental evidence of streamwise vortices as finite amplitude solutions in transitional plane Couette flow. *Phys. Fluids* **10** (10), 2597–2607.

Cantwell, B.J. 2019 A universal velocity profile for smooth wall pipe flow. *J. Fluid Mech.* **878**, 834–874.

Cheng, W., Pullin, D.I. & Samtaney, R. 2022 Wall-resolved and wall-modelled large-eddy simulation of plane Couette flow. *J. Fluid Mech.* **934**, A19.

https://doi.org/10.1017/jfm.2022.1023 Published online by Cambridge University Press

CHOI, Y.K., LEE, J.H. & HWANG, J. 2021 Direct numerical simulation of a turbulent plane Couette–Poiseuille flow with zero-mean shear. *Intl J. Heat Fluid Flow* **90**, 108836.

CHUNG, D. & PULLIN, D.I. 2009 Large-eddy simulation and wall modelling of turbulent channel flow. *J. Fluid Mech.* **631**, 281–309.

COLEMAN, G.N., PIROZZOLI, S., QUADRIO, M. & SPALART, P.R. 2017 Direct numerical simulation and theory of a wall-bounded flow with zero skin friction. *Flow Turbul. Combust.* **99**, 553–564.

COULIOU, M. & MONCHAUX, R. 2015 Large-scale flows in transitional plane Couette flow: a key ingredient of the spot growth mechanism. *Phys. Fluids* **27**, 034101.

ELTELBANY, M.M.M. & REYNOLDS, A.J. 1980 Velocity distributions in plane turbulent channel flows. *J. Fluid Mech.* **100** (SEP), 1–29.

ELTELBANY, M.M.M. & REYNOLDS, A.J. 1981 Turbulence in plane channel flows. *J. Fluid Mech.* **111** (OCT), 283–318.

GANDÍA-BARBERÁ, S., HOYAS, S., OBERLACK, M. & KRAHEBERGER, S. 2018 Letter: the link between the Reynolds shear stress and the large structures of turbulent Couette–Poiseuille flow. *Phys. Fluids* **30** (4), 041702.

JONES, M.B., MARUSIC, I. & PERRY, A.E. 2001 Evolution and structure of sink-flow turbulent boundary layers. *J. Fluid Mech.* **428**, 1–27.

KIM, J.H., HWANG, J.H., LEE, Y.M. & LEE, J.H. 2020 Direct numerical simulation of a turbulent Couette–Poiseuille flow. Part 2: large- and very-large-scale motions. *Intl J. Heat Fluid Flow* **86**, 108687.

KIM, J.H. & LEE, J.H. 2018 Direct numerical simulation of a turbulent Couette–Poiseuille flow: turbulent statistics. *Intl J. Heat Fluid Flow* **72**, 288–303.

KLOTZ, L., LEMOULT, G., FRONTCZAK, I., TUCKERMAN, L.S. & WESFREID, J.E. 2017 Couette–Poiseuille flow experiment with zero mean advection velocity: subcritical transition to turbulence. *Phys. Rev. Fluids* **2**, 043904.

LEE, M. & MOSER, R.D. 2015 Direct numerical simulation of turbulent channel flow up to $Re_\tau \approx 5200$. *J. Fluid Mech.* **774**, 395–415.

LEE, M. & MOSER, R.D. 2018 Extreme-scale motions in turbulent plane Couette flows. *J. Fluid Mech.* **842**, 128–145.

LUNDGREN, T.S. 1982 Strained spiral vortex model for turbulent fine structure. *Phys. Fluids* **25**, 2193–2203.

NAGIB, H.M., CHAUHAN, K.A. & MONKEWITZ, P.A. 2007 Approach to an asymptotic state for zero pressure gradient turbulent boundary layers. *Phil. Trans. R. Soc. Lond.* A **365**, 755–770.

NAKABAYASHI, K., KITOH, O. & KATOH, Y. 2004 Similarity laws of velocity profiles and turbulence characteristics of Couette–Poiseuille turbulent flows. *J. Fluid Mech.* **507**, 43–69.

PIROZZOLI, S., BERNARDINI, M. & ORLANDI, P. 2011 Large-scale motions and inner/outer layer interactions in turbulent Couette–Poiseuille flows. *J. Fluid Mech.* **680**, 534–563.

PIROZZOLI, S., BERNARDINI, M. & ORLANDI, P. 2014 Turbulence statistics in Couette flow at high Reynolds number. *J. Fluid Mech.* **758**, 327–343.

PULLIN, D.I., INOUE, M. & SAITO, N. 2013 On the asymptotic state of high Reynolds number, smooth-wall turbulent flows. *Phys. Fluids* **25**, 015116.

SAITO, N., PULLIN, D.I. & INOUE, M. 2012 Large eddy simulation of smooth-wall, transitional and fully rough-wall channel flow. *Phys. Fluids* **24** (7), 075103.

SCHULTZ, M.P. & FLACK, K.A. 2013 Reynolds-number scaling of turbulent channel flow. *Phys. Fluids* **25**, 025104.

STRATFORD, B.S. 1959 The prediction of separation of the turbulent boundary layer. *J. Fluid Mech.* **5** (1), 1–16.

SUBRAHMANYAM, M.A., CANTWELL, B.J. & ALONSO, J.J. 2022 A universal velocity profile for turbulent wall flows including adverse pressure gradient boundary layers. *J. Fluid Mech.* **933**, A16.

THURLOW, E.M. & KLEWICKI, J.C. 2000 Experimental study of turbulent Poiseuille–Couette flow. *Phys. Fluids* **12** (4), 865–875.

TILLMARK, N. & ALFREDSSON, P.H. 1992 Experiments on transition in plane Couette flow. *J. Fluid Mech.* **235**, 89–102.

WEI, T., FIFE, P. & KLEWICKI, J. 2007 On scaling the mean momentum balance and its solutions in turbulent Couette–Poiseuille flow. *J. Fluid Mech.* **573**, 371–398.

YANG, K., ZHAO, L. & ANDERSSON, H.I. 2017 Turbulent Couette–Poiseuille flow with zero wall shear. *Intl J. Heat Fluid Flow* **63**, 14–27.

https://doi.org/10.1017/jfm.2022.1023 Published online by Cambridge University Press